Macroscopic modelling and a moving mesh method for liquid thin films with moving contact lines on general substrates

Si Xiao[1], Xianmin Xu[2,*]

[1] *School of Mathematics and Statistics, Fuzhou University, Fuzhou 350108, Fujian, China*
[2] *State Key Laboratory of Mathematical Sciences, ICMSEC, NCMIS, Academy of Mathematics and Systems Science, Chinese Academy of Sciences, Beijing 100190, China*

Abstract. Thin liquid films with contact lines are common in nature and in engineering applications. The existence of free boundaries and singularities poses significant challenges for both modeling and computation. In this work, we present a unified framework for the derivation and numerical approximation of a fourth-order thin film equation with mesoscopic dynamic boundary conditions. The reduced model is systematically derived using the Onsager variational principle in conjunction with lubrication theory, yielding a thermodynamically consistent formulation that accounts for capillarity, gravity, and external force. To solve the resulting free boundary problem, we develop adaptive moving mesh methods based on a discrete Onsager variational principle, including a stabilized semi-implicit scheme to improve computational efficiency. Numerical results confirm the optimal convergence of the proposed methods and accurately capture key wetting behaviors, including contact angle hysteresis on rough substrates. This work offers a robust framework for simulating thin film flows with complex geometries.

AMS subject classifications: 35R35, 35K65, 62F35, 65M60, 65M65, 74K35, 82C35

Key words: thin film equation, moving mesh method, Onsager variational principle, free boundary problem.

1 Introduction

The study of interfacial fluid dynamics plays an important role in soft matter physics and engineering sciences, with wetting phenomena representing one of its most ubiquitous yet challenging manifestations [1–4]. In particular, the dynamics of thin liquid films, where the size of the flow domain in one direction is essentially smaller in comparison

*Corresponding author. *Email address:* xiaosi@fzu.edu.cn (S. Xiao), xmxu@lsec.cc.ac.cn (X. Xu)

with that in the other directions, arise in a variety of natural and industrial processes, including tear film on the eye, coating flows in manufacturing, and microfluidic patterning in biomedical devices [1]. Understanding the behavior of such films with moving contact lines is essential for both fundamental science and practical applications.

In such thin film configurations, the classical Navier–Stokes equations can be systematically reduced via the lubrication approximation, yielding a class of fourth-order nonlinear degenerate parabolic equations known as the fourth-order thin film equation. A general form of the thin film equation is given by

$$\partial_t h + \nabla \cdot (h^n \nabla \Delta h) = 0, \quad n > 0, \tag{1.1}$$

where h denotes the film height, n is a positive parameter. This formulation generalizes numerous classical flow problems [1, 5–9]. The case $n = 1$ corresponds to flow of two immiscible fluids in a Hele-Shaw cell (two parallel plates separated by a narrow gap) or flow in a porous medium. In the case where $n = 3$, the equation characterizes the spreading of a liquid film along a solid substrate. It also applies to the case $n = 2$ where the fluid is able to "slip" over the solid.

From a mathematical standpoint, thin film equations represent a nonlinear generalization of the biharmonic equation and a fourth-order analogue of the porous medium equation. Analogous to the well-established theoretical investigations into the properties of the porous medium equation, including the maximum principle, well-posedness of solutions, and finite propagation speed at the boundary, the thin film equation has been the subject of extensive study (e.g., [10–18]). Nevertheless, the development of the mathematical theory for such fourth-order degenerate equations poses significantly greater challenges compared to their second-order counterparts. For example, for sufficiently large values of n, solutions of the thin film equation (1.1) exhibit positive property. However, for smaller values of n, computational evidence suggests the emergence of singularities, characterized by h tending to zero in finite time. This phenomenon introduces substantial difficulties in the formulation and analysis of a weak solution framework for these equations [5]. Early numerical studies assume the thickness is always positive and aim to develop positivity-preserving and convergent schemes for lubrication-type equations in fixed domain (without moving contact lines) [19, 20].

Physically, the case $n = 3$ in the thin film equation arises from the Navier-Stokes equation coupled with the classical no-slip boundary condition. However, this formulation leads to the so-called moving contact line paradox [21, 22], wherein the shear stress diverges near the contact line, implying unphysical infinite energy dissipation. Two principal regularization strategies have been developed to address this singularity. The precursor film model postulates a microscopically thin, stable layer ahead of the apparent contact line, regularized through a disjoining pressure potential [23–27]. Alternatively, the slip model modifies the boundary condition to permit finite slip at the solid-liquid interface, thereby maintaining a sharp contact line and giving rise to a free boundary formulation [21, 28–37].

The precursor film model eliminates the need for explicit moving boundary conditions, thereby facilitating the handling of topological changes such as droplet breakup and coalescence. However, this approach typically requires the grid resolution near the contact line to be smaller than the precursor film thickness, which can introduce computational inefficiencies, particularly in higher-dimensional settings [38–41]. By contrast, the slip model is more frequently employed in theoretical analysis but inherently involves moving boundaries. In this context, the thin-film equation is formulated as a free boundary problem. To address such problems, approaches such as arbitrary Lagrangian-Eulerian (ALE) methods [42–44] or alternative coordinate transformation techniques [45–48] are commonly utilized. However, the slip length in the model is usually of nano scale. This induces significant challenges for quantitative numerical simulations for complicated thin film problems. Especially when there exist rough substrates, the complexity of the boundary conditions further increases, highlighting the need for coarse-graining models and efficient and robust numerical methods tailored to such scenarios.

A natural and systematic framework for addressing such challenges is provided by the Onsager variational principle which is a fundamental concept in nonequilibrium thermodynamics [49, 50]. The Onsager variational principle formulates the evolution of dissipative systems as a minimization problem of a Rayleighian functional, which combines the time derivative of the system's free energy and the dissipation potential. Recent studies have demonstrated that the Onsager variational principle is not only effective for the derivation of coarse-grained models in complex systems [51–57] but also advantageous for the construction of numerical methods [58–61]. In particular, for free boundary problems arising in interfacial fluid dynamics, the Onsager variational principle offers a unified approach to model reduction and numerical scheme design.

In this paper, we develop a coarse-graining model and an efficient moving mesh numerical method for complicated thin film problems with moving contact lines. Leveraging the Onsager variational principle and lubrication approximation theory, we derive a reduced model in the form of a fourth-order thin film equation that naturally incorporates the effects of capillary forces, gravitational forces, and external fields, along with dynamic contact line conditions. Building upon the discrete Onsager variational principle, and drawing inspiration from recent developments in porous medium flows [60], we construct an explicit numerical method as well as a stabilized semi-implicit scheme to enhance computational performance. Numerical experiments demonstrate that both methods achieve optimal convergence rates in the L^2 norm. Moreover, the stabilized semi-implicit scheme significantly relaxes time step restrictions compared to the explicit one. The numerical results also validate several widely accepted predictions regarding advancing and receding contact angles in droplet wetting on rough substrates, providing further insights into these complex phenomena.

The remainder of the paper is organized as follows. In Section 2, we systematically derive the fourth-order thin film equations along with the associated dynamic boundary conditions on rough substrates, based on the Onsager variational principle and lubrication approximation theory. Section 3 is devoted to the construction of moving mesh

numerical schemes derived from the Onsager variational principle, where a stabilized semi-implicit method is further introduced to address the time step restrictions of explicit discretizations. Section 4 presents a series of numerical experiments that validate the accuracy and efficiency of the proposed methods. Finally, Section 5 concludes the paper with a summary and discussion of future research directions.

2 Macroscopic modelling for the thin films with moving contact lines

In this section, we develop a macroscopic model for the motion of incompressible Newtonian liquid film on a general substrate. Suppose that the height of the film is much smaller than its radius. We derive the thin film equation and its corresponding dynamic boundary conditions using the Onsager variational principle. For simplicity, we consider a two-dimensional problem.

As shown in Figure 1, we assume that the boundary of the substrate is given by $z=R(x)$, and the liquid profile at time t is located at $z=h(x,t)=H(x,t)+R(x)$, where $H(x,t)$ represents the thickness of liquid from the liquid-vapor interface to the substrate. Let γ, γ_{SV} and γ_{SL} be the surface tensions of the liquid-vapor interface Γ_{LV}, solid-vapor

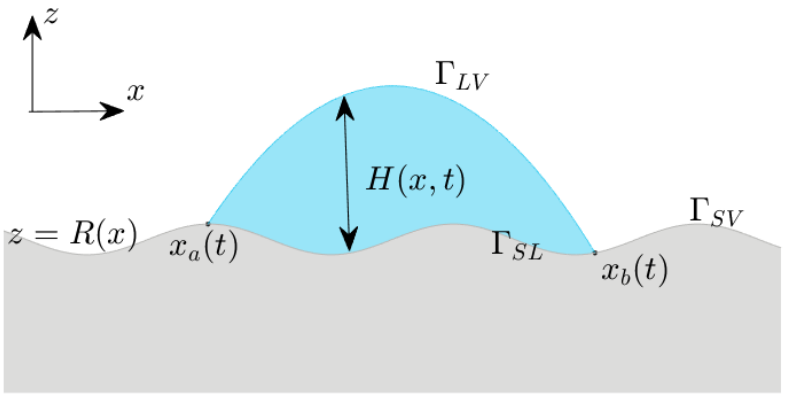

Figure 1: The shape of droplet on a rough surface.

interface Γ_{SV} and solid-liquid interface Γ_{SL}, respectively. In this setting, the three-phase contact points are represented as $(x_a(t),R(x_a))$ and $(x_b(t),R(x_b))$ at time t. The equilibrium contact angle θ_Y satisfies the Young equation:

$$\gamma_{SV}-\gamma_{SL}=\gamma\cos\theta_Y. \tag{2.1}$$

As shown in Figure 2, the local dynamic contact angles θ_d^a and θ_d^b and the apparent contact angles θ_a and θ_b satisfy the following relationship:

$$\theta_d^a=\theta_a-\theta_g^a,\quad \theta_d^b=\theta_b+\theta_g^b, \tag{2.2}$$

where θ_a and θ_b are given by $\theta_a = \arctan\partial_x h(x_a,t)$ and $\theta_b = \arctan(-\partial_x h(x_b,t))$, and θ_g characterizes the local slope of the oscillating substrate at the contact line and is given by $\theta_g = \arctan\partial_x R$. We set $\theta_g^a = \theta_g(x_a)$ and $\theta_g^b = \theta_g(x_b)$. Notice that the apparent contact

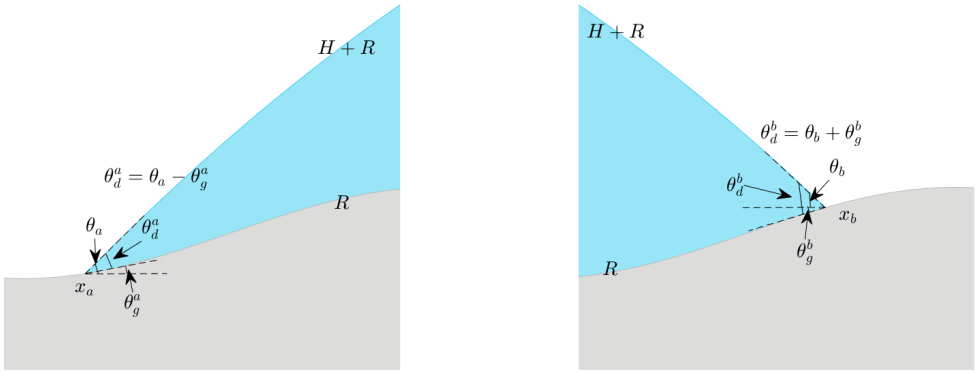

Figure 2: The relationship of contact angles.

angle θ_a is obtained by rotating counterclockwise from the positive horizontal x-axis to the liquid interface. And the apparent contact angle θ_b is obtained by rotating clockwise from the negative horizontal x-axis to the liquid interface. The sign of θ_g depends on the value of $\partial_x R(x)$. By simple calculations, we derive that

$$\cos\theta_b = \frac{1}{\sqrt{1+(\partial_x h(x_b))^2}}; \quad \sin\theta_b = -\frac{\partial_x h(x_b)}{\sqrt{1+(\partial_x h(x_b))^2}}, \tag{2.3}$$

$$\cos\theta_a = \frac{1}{\sqrt{1+(\partial_x h(x_a))^2}}; \quad \sin\theta_a = \frac{\partial_x h(x_a)}{\sqrt{1+(\partial_x h(x_a))^2}}, \tag{2.4}$$

$$\cos\theta_g = \frac{1}{\sqrt{1+(\partial_x R)^2}}; \qquad \sin\theta_g = \frac{\partial_x R}{\sqrt{1+(\partial_x R)^2}}. \tag{2.5}$$

The geometric constraints for the liquid at the contact points are as follows:

$$H = 0 \quad \text{when } x = x_a(t) \text{ or } x = x_b(t). \tag{2.6}$$

By taking time derivative to the above equation, we are led to

$$\partial_t H = -\partial_x H\dot{x} \quad \text{when } x = x_a(t) \text{ or } x = x_b(t). \tag{2.7}$$

We will derive the equation for $H(x,t)$ by the Onsager variational principle below.

2.1 The total energy

We first consider the total free energy $\mathcal{E}$ in the system, which is composed of three parts,

$$\mathcal{E} = \mathcal{E}_s + \mathcal{E}_g + \mathcal{E}_f, \tag{2.8}$$

where $\mathcal{E}_s$, $\mathcal{E}_g$ and $\mathcal{E}_f$ are the surface energy, the gravitational potential energy and the external potential energy, respectively.

The surface energy $\mathcal{E}_s$ of the system is given by

$$\mathcal{E}_s = \int_{\Gamma_{SV}} \gamma_{SV} ds + \int_{\Gamma_{SL}} \gamma_{SL} ds + \int_{\Gamma_{LV}} \gamma ds. \tag{2.9}$$

By using the Young equation (2.1), we have

$$\mathcal{E}_s = \int_{\Gamma_{SV}\cup\Gamma_{SL}} \gamma_{SV} ds + \int_{x_a}^{x_b} -\gamma\cos\theta_Y \sqrt{1+(\partial_x R)^2} dx + \int_{x_a}^{x_b} \gamma\sqrt{1+(\partial_x(H+R))^2} dx. \tag{2.10}$$

The gravitational potential energy $\mathcal{E}_g$ of the system along the z-axis can be expressed as follows

$$\mathcal{E}_g = \int_{x_a}^{x_b} \int_{R(x)}^{H(x,t)+R(x)} \rho g z dz dx = \int_{x_a}^{x_b} \frac{1}{2}\rho g((H+R)^2 - R^2) dx, \tag{2.11}$$

where ρ is the density of the liquid, and g is the gravitational acceleration.

If an external potential is applied to the liquid along the x-axis, the corresponding external potential energy $\mathcal{E}_f$ can be expressed as

$$\mathcal{E}_f = \int_{x_a}^{x_b} \int_{R(x)}^{H(x,t)+R(x)} -\rho f x dz dx = \int_{x_a}^{x_b} -\rho f x H dx. \tag{2.12}$$

To use the Onsager variational principle, we need to compute the rate of change of total energy with respect to t. By using the contact angle relations (2.3)-(2.5) and the boundary condition (2.7), we obtain the rate of change of the surface energy $\dot{\mathcal{E}}_s$

$$\begin{aligned} \dot{\mathcal{E}}_s = &- \int_{x_a}^{x_b} \gamma \frac{\partial_{xx}(H+R)}{(1+(\partial_x(H+R))^2)^{3/2}} \partial_t H dx \\ &- \gamma(\cos\theta_g^b)^{-1}(\cos\theta_Y - \cos\theta_d^b)\dot{x}_b + \gamma(\cos\theta_g^a)^{-1}(\cos\theta_Y - \cos\theta_d^a)\dot{x}_a. \end{aligned} \tag{2.13}$$

In thin film regime, we assume that $|\partial_x(H+R)| \ll 1$. This leads to the approximation of the curvature $\frac{\partial_{xx}(H+R)}{(1+(\partial_x(H+R))^2)^{3/2}} \approx \partial_{xx}(H+R)$, so that

$$\begin{aligned} \dot{\mathcal{E}}_s \approx &- \int_{x_a}^{x_b} \gamma \partial_{xx}(H+R) \partial_t H dx \\ &- \gamma(\cos\theta_g^b)^{-1}(\cos\theta_Y - \cos\theta_d^b)\dot{x}_b + \gamma(\cos\theta_g^a)^{-1}(\cos\theta_Y - \cos\theta_d^a)\dot{x}_a. \end{aligned} \tag{2.14}$$

Then, by direct calculations from (2.11), the rate of change of the gravitational potential energy $\dot{\mathcal{E}}_g$ is given by

$$\dot{\mathcal{E}}_g = \int_{x_a}^{x_b} \rho g (H+R) \partial_t H dx. \tag{2.15}$$

Similarly, the rate of change of the external potential energy $\dot{\mathcal{E}}_f$ is given by

$$\dot{\mathcal{E}}_f = -\int_{x_a}^{x_b} \rho f x \partial_t H dx. \tag{2.16}$$

2.2 The dissipation function

To derive the dynamic equation for the thin film, we then calculate the total energy dissipation in the system. It is known that the standard no-slip boundary condition leads to infinite energy dissipation near the contact line. This is the so-called moving contact line paradox. To cure the paradox, a general way is to consider slip of liquid near the contact lines [2]. Notice that the slip length is generally of nano-meter scale. It is not realistic to resolve the scale in numerical simulations. Therefore, we divide the fluid into three distinct regions: the bulk region far from the contact line, the meso-scale wedge-shaped region near the contact line with a characteristic length l, and the contact line region within a microscopic scale $l_c \sim 1nm$. We calculate the energy dissipation in the regions individually and approximately.

Firstly, we compute the viscous energy dissipation in the bulk region, where the lubrication approximation and the no-slip boundary condition can be used. By the lubrication approximation theory, the viscous energy dissipation is given by

$$\Psi_b = \int_{x_a+l}^{x_b-l} \frac{3\mu}{H} v^2 dx, \tag{2.17}$$

where $v(x,t)$ is the depth-averaged horizontal fluid velocity.

Secondly, we consider the viscous energy dissipation in the wedge-shape region. In this case, the lubrication approximation does not apply. When the contact angle is small, the dissipation can be approximated by [2]

$$\Phi_{w1} = \frac{3\mu}{\theta_d} |\ln\zeta| v_{ct}^2, \tag{2.18}$$

where the dimensionless coefficient $\zeta = l/l_c$ is a dimensionless cut-off parameter, θ_d is the dynamic contact angle, and v_{ct} is the velocity of the fluid near the contact line. When the contact angle is large, the energy dissipation in the wedge-shape region can be calculated approximately by solving the Stokes equation with some certain boundary conditions (c.f. [62]), which is given by

$$\Psi_{w2} = \frac{2\mu |\ln\zeta| \sin^2\theta_d}{\theta_d - \sin\theta_d \cos\theta_d} v_{ct}^2. \tag{2.19}$$

When $\theta_d \ll 1$, equation (2.19) will reduce to equation (2.18). We adopt equation (2.19) to describe the energy dissipation in wedge-shape region in this paper.

Lastly, we consider the viscous energy dissipation at the contact lines region. This dissipation is caused by the friction of the contact lines. The local dissipation is given by

$$\Psi_c = \xi_0 v_{ct}^2, \tag{2.20}$$

where ξ_0 is the viscosity coefficient of the contact lines. The coefficient ξ_0 has been directly measured by experiments in [63], which can be approximated by $\alpha\mu$ with α being a positive parameter.

Combining the above results, we obtain the energy dissipation function of the system, which is defined as half of the energy dissipated in the system in unit time, as

$$\Phi(H;v,\dot{x}_a,\dot{x}_b) = \frac{1}{2}(\Psi_b + \Psi_{w2} + \Psi_c). \tag{2.21}$$

In our settings, there are two contact points, x_a and x_b. The contact point velocity v_{ct} on a rough substrate is related to $\dot{x}$ by $v_{ct}\cos\theta_g = \dot{x}$. Direct calculations give

$$\Phi(H;v,\dot{x}_a,\dot{x}_b) = \frac{1}{2}\int_{x_a+l}^{x_b-l} \frac{3\mu}{H} v^2 dx + \frac{\mu}{2\cos^2\theta_g^b}\mathcal{F}(\theta_d^b)\dot{x}_b^2 + \frac{\mu}{2\cos^2\theta_g^a}\mathcal{F}(\theta_d^a)\dot{x}_a^2, \tag{2.22}$$

where

$$\mathcal{F}(\theta_d) = \frac{2|\ln\zeta|\sin^2\theta_d}{\theta_d - \sin\theta_d\cos\theta_d} + \alpha. \tag{2.23}$$

2.3 The dynamic equation

We will derive the dynamic equation for the fluid film on a general substrate using Onsager variational principle.

Assuming that the fluid does not evaporate, then it satisfies the volume conservation condition, i.e.

$$\partial_t H + \partial_x(Hv) = 0. \tag{2.24}$$

We define the Rayleighian functional

$$\mathcal{R}(H;\partial_t H,v,\dot{x}_a,\dot{x}_b) = \Phi(H;v,\dot{x}_a,\dot{x}_b) + \dot{\mathcal{E}}(H;\partial_t H,\dot{x}_a,\dot{x}_b). \tag{2.25}$$

Notice that $l \ll 1$, we can write

$$\begin{aligned}\dot{\mathcal{E}} \approx \int_{x_a+l}^{x_b-l} &\big(-\gamma\partial_{xx}(H+R) + \rho g(H+R) - \rho f x\big)\partial_t H dx \\ &-\gamma(\cos\theta_g^b)^{-1}(\cos\theta_Y - \cos\theta_d^b)\dot{x}_b + \gamma(\cos\theta_g^a)^{-1}(\cos\theta_Y - \cos\theta_d^a)\dot{x}_a\end{aligned}$$

By the Onsager variational principle, the dynamic equation will be obtained by minimizing the Rayleighian functional under the constraint of volume conservation, i.e.,

$$\begin{aligned} &\min_{\partial_t H, v, \dot{x}_a, \dot{x}_b} \mathcal{R}(H; \partial_t H, v, \dot{x}_a, \dot{x}_b) \\ &s.t. \quad \partial_t H + \partial_x (Hv) = 0. \end{aligned} \tag{2.26}$$

To derive the dynamic equation, we define the modified Rayleighian functional by introducing Lagrange multiplier $\lambda(x)$,

$$\tilde{\mathcal{R}} = \Phi(v, \dot{x}_a, \dot{x}_b) + \dot{\mathcal{E}}(H; \partial_t H, \dot{x}_a, \dot{x}_b) - \int_{x_a+l}^{x_b-l} \lambda(x)(\partial_t H + \partial_x (Hv))dx. \tag{2.27}$$

The Euler-Lagrange equation corresponding to the variational problem (2.26) is obtained by setting the first-order variation of $\tilde{\mathcal{R}}$ to be zero, i.e. $\delta\tilde{\mathcal{R}} = 0$. This leads to

$$\begin{cases} -\gamma \partial_{xx}(H+R) + \rho g(H+R) - \rho f x - \lambda = 0, \\ \frac{3\mu}{H} v + H \partial_x \lambda = 0, \\ \partial_t H + \partial_x (Hv) = 0. \end{cases} \tag{2.28}$$

in (x_a+l, x_b-l) and the boundary conditions

$$\begin{cases} \dot{x}_a = -\gamma \mu^{-1} \cos\theta_g^a (\mathcal{F}(\theta_d^a))^{-1} (\cos\theta_Y - \cos\theta_d^a), \\ \dot{x}_b = \gamma \mu^{-1} \cos\theta_g^b (\mathcal{F}(\theta_d^b))^{-1} (\cos\theta_Y - \cos\theta_d^b). \end{cases} \tag{2.29}$$

Here the Lagrange multiplier λ represents the pressure in the liquid. The first equation in (2.28) shows a force balance on the surface of the thin film. The second equation in (2.28) implies a Darcy's law for the average velocity. From these equations, we obtain a fourth-order thin film equation

$$\partial_t H + \frac{1}{3\mu} \partial_x (H^3 (\gamma \partial_{xxx}(H+R) - \rho g \partial_x (H+R) + \rho f)) = 0. \tag{2.30}$$

When the substrate is flat (i.e. $R(x) = 0$), then height function $H(x,t) = h(x,t)$. In this case, the equation (2.30) is reduced to the standard thin film fluid model on a flat substrate. Finally, to close the system, we need also use the geometric constraints that

$$H(x_a+l, t) = l \tan\theta_d^a, \quad H(x_b-l, t) = l \tan\theta_d^b,$$

where we have used the fact that $H(x_a, t) = H(x_b, t) = 0$ and the interface is approximated by a straight line in the vicinity of the contact points. In addition, we will also need the consitency condition that $v(x_a) = \dot{x}_a$ and $v(x_b) = \dot{x}_b$.

2.4 The dimensionless equations

In order to facilitate numerical implementation, we nondimensionalize the thin film equation. Let L represent the characteristic length of the droplet in the x-direction. The corresponding dimensionless length, height, and time are denoted by

$$x = L\bar{x}, \quad H = L\bar{H}, \quad t = T\bar{t},$$

where the characteristic time $T = \frac{3\mu L}{\gamma}$. Introduce two dimensionless parameters, B_o and B_x, which respectively represent the magnitude of gravitational effects in the vertical direction and external forces in the horizontal direction,

$$B_o = \frac{\rho g L^2}{\gamma}, \quad B_x = \frac{\rho f L^2}{\gamma}.$$

We can derive the dimensionless fourth-order thin film equation

$$\partial_{\bar{t}}\bar{H} + \partial_{\bar{x}}(\bar{H}^3(\partial_{\bar{x}\bar{x}\bar{x}}(\bar{H}+\bar{R}) - B_o\partial_{\bar{x}}(\bar{H}+\bar{R}) + B_x)) = 0. \tag{2.31}$$

For simplicity in presentation, we will drop the bar on the dimensionless variables in the following context. The dimensionless problem is given by

$$\begin{cases} \partial_t H + \partial_x(H^3(\partial_{xxx}(H+R) - B_o\partial_x(H+R) + B_x)) = 0, & x \in I^l(t), t > 0, \\ H(x_a(t)+l,t) = l\tan\theta_d^a, \quad H(x_b(t)-l,t) = l\tan\theta_d^b, & t > 0, \\ \dot{x}_a = 3\cos^2\theta_g^a(\mathcal{F}(\theta_d^a))^{-1}\varsigma(x_a), & t > 0, \\ \dot{x}_b = -3\cos^2\theta_g^b(\mathcal{F}(\theta_d^b))^{-1}\varsigma(x_b), & t > 0, \\ H(x,0) = H^0(x), & x \in I^l(0). \end{cases} \tag{2.32}$$

Here $I^l(t) = [x_a(t)+l, x_b(t)-l]$ is the region where the fluid occupies (without the vicinity of the contact line), and

$$\varsigma(x) = -\cos\theta_Y(\cos\theta_g)^{-1} + 1 + \frac{1}{2}(\partial_x(H+R)(x))^2 - \partial_x(H+R)(x)\partial_x H(x).$$

The free boundary conditions and the given initial condition in (2.32) are sufficient to make the fourth-order thin film equation well-defined. However, rigorously proving the well-posedness of the solution remains a challenging mathematical problem [64].

For later use, we introduce the dimensionless energy and dissipation functions below. In the dimensionless form, the dimensionless surface energy $\mathcal{E}_s$, the gravitational potential energy $\mathcal{E}_g$ and the external potential $\mathcal{E}_f$ are as follows

$$\begin{aligned} \mathcal{E}_s &= \int_{x_a}^{x_b} 1 + \frac{1}{2}(\partial_x(H+R))^2 dx - \cos\theta_Y \int_{x_a}^{x_b} \sqrt{1+(\partial_x R)^2}\, dx, \\ \mathcal{E}_g &= \int_{x_a}^{x_b} \frac{1}{2} B_o((H+R)^2 - R^2) dx, \\ \mathcal{E}_f &= -\int_{x_a}^{x_b} B_x x H dx. \end{aligned} \tag{2.33}$$

The dimensionless dissipation function is expressed as

$$\Phi(H;v,\dot{x}_a,\dot{x}_b)=\frac{1}{2}\int_{x_a+l}^{x_b-l}\frac{v^2}{H}dx+\frac{1}{6\cos^2\theta_g^a}\mathcal{F}(\theta_d^a)\dot{x}_a^2+\frac{1}{6\cos^2\theta_g^b}\mathcal{F}(\theta_d^b)\dot{x}_b^2. \tag{2.34}$$

3 The moving mesh methods

In this section, we propose an efficient numerical method for solving the fourth-order thin film equation (2.32). Notice that the equation is a nonlinear fourth-order partial differential equations with dynamic equation. Numerical solution to the equation is highly challenging. We construct a moving finite element method by using the Onsager variational principle as an approximation tool.

3.1 Semi-discretization

Introduce a partition for the interval $I(t)=[x_a(t),x_b(t)]$,

$$X(t):=\{x_a(t)=x_0(t)<x_1(t)<\cdots<x_N(t)=x_b(t)\}, \tag{3.1}$$

where the knots may change the position with respect to time. Denote by $I_i(t)=[x_{i-1}(t),x_i(t)]$ the sub-interval in the partition $X(t)$. Then we can define the finite element space V_h^t as

$$V_h^t:=\{u_h\in C[I(t)]:u_h \text{ is linear in } I_i(t),\quad \forall i=1,...,N\}.$$

Denote the space $V_{h,0}^t=\{u_h\in V_h^t:u_h(x_a)=u_h(x_b)=0\}$, then for any function $H_h(x,t)\in V_{h,0}^t$, it can be expressed as

$$H_h(x,t)=\sum_{i=1}^{N-1}H_i(t)\phi_i(x,t),$$

where the function $\phi_i(x,t)$ is a finite element basis function associated with x_i, i.e.

$$\phi_i(x,t)=\phi_i^l+\phi^r=\frac{x-x_{i-1}(t)}{x_i(t)-x_{i-1}(t)}\chi_{I_i}(x)+\frac{x_{i+1}(t)-x}{x_{i+1}(t)-x_i(t)}\chi_{I_{i+1}}(x), \tag{3.2}$$

where χ_{I_i} is the characteristic function corresponding to I_i. The time derivative and space derivative of $H_h(x,t)$ are respectively given by

$$\begin{aligned}\partial_t H_h&=\sum_{i=1}^{N-1}\dot{H}_i(t)\phi_i(x,t)+\sum_{i=0}^{N}\dot{x}_i(t)\psi_i(x,t),\\ \partial_x H_h&=\sum_{i=1}^{N-1}H_i(t)\partial_x\phi_i(x,t),\end{aligned}$$

where $\psi_k=\frac{\partial H_h}{\partial x_k}$. Denote by $\mathbf{H}=(H_1(t),...,H_{N-1}(t))^T$ and $\mathbf{x}=(x_0(t),...,x_N(t))^T$. We will derive a dynamic equation for $\mathbf{H}$ and $\mathbf{x}$ by using the Onsager variational principle.

Firstly, we discretize the energy functionals in (2.33) and as follows

$$\mathcal{E}_h(\mathbf{H},\mathbf{x};\dot{\mathbf{H}},\dot{\mathbf{x}}) = \mathcal{E}_{s,h}(\mathbf{H},\mathbf{x};\dot{\mathbf{H}},\dot{\mathbf{x}}) + \mathcal{E}_{g,h}(\mathbf{H},\mathbf{x};\dot{\mathbf{H}},\dot{\mathbf{x}}) + \mathcal{E}_{f,h}(\mathbf{H},\mathbf{x};\dot{\mathbf{H}},\dot{\mathbf{x}}),$$

where the discrete $\mathcal{E}_{s,h}$, $\mathcal{E}_{g,h}$ and $\mathcal{E}_{f,h}$ are respectively given by

$$\begin{aligned}
\mathcal{E}_{s,h} &= \sum_{i=1}^{N}\Big(\int_{I_i(t)} 1+\frac{1}{2}(\partial_x(H_h+R))^2 dx - \cos\theta_Y \int_{I_i(t)} \sqrt{1+(\partial_x R)^2}dx\Big),\\
\mathcal{E}_{g,h} &= \sum_{i=1}^{N}\int_{I_i(t)} \frac{1}{2}B_o((H_h+R)^2-R^2)dx,\\
\mathcal{E}_{f,h} &= -\sum_{i=1}^{N}\int_{I_i(t)} B_x x H_h dx.
\end{aligned}$$

The rate of change of discrete energy is calculated directly as

$$\dot{\mathcal{E}}_h(\mathbf{H},\mathbf{x};\dot{\mathbf{H}},\dot{\mathbf{x}}) = \sum_{i=1}^{N-1}\frac{\partial \mathcal{E}_h}{\partial H_i}\dot{H}_i + \sum_{i=0}^{N}\frac{\partial \mathcal{E}_h}{\partial x_i}\dot{x}_i, \tag{3.3}$$

where

$$\begin{aligned}
\frac{\partial \mathcal{E}_h}{\partial H_i} &= \int_{I(t)} \partial_x(H_h+R)\partial_x\phi_i dx + \int_{I(t)} B_o(H_h+R)\phi_i dx + \int_{I(t)} -B_x x\phi_i dx,\\
&\qquad\qquad i=1,...,N;\\
\frac{\partial \mathcal{E}_h}{\partial x_i} &= \int_{I(t)} \partial_x(H_h+R)\partial_x\psi_i dx + \int_{I(t)} B_o(H_h+R)\psi_i dx + \int_{I(t)} -B_x x\psi_i dx,\\
&\qquad\qquad i=1,...,N;\\
\frac{\partial \mathcal{E}_h}{\partial x_0} &= \int_{I(t)} \partial_x(H_h+R)\partial_x\psi_0 dx + \int_{I(t)} B_o(H_h+R)\psi_0 dx + \int_{I(t)} -B_x x\psi_0 dx\\
&\quad +\cos\theta_Y\sqrt{1+(\partial_x R(x_0))^2} - (1+\frac{1}{2}\partial_x(H_h+R)(x_0));\\
\frac{\partial \mathcal{E}_h}{\partial x_N} &= \int_{I(t)} \partial_x(H_h+R)\partial_x\psi_N dx + \int_{I(t)} B_o(H_h+R)\psi_N dx + \int_{I(t)} -B_x x\psi_N dx\\
&\quad -\cos\theta_Y\sqrt{1+(\partial_x R(x_N))^2} + (1+\frac{1}{2}\partial_x(H_h+R)(x_N)).
\end{aligned}$$

Here that the integral in above equation vanishes out of the support of the basis function ϕ_i or ψ_i.

Secondly, in order to discretize the dissipation function, we need to pay more attention to the two boundary intervals. Notice that the integral term $\int_I \frac{v_h(x,t)^2}{2H_h(x,t)}dx$ is singular at the boundary points(contact points). We need truncate the integral as for the continuous case, where we introduce a cut-off parameter $l \ll 1$ and do integration in the bulk region

$\tilde{I}=[x_a(t)+l,x_b(t)-l]$. Therefore, to derive the discrete energy dissipation, we replace I_1 and I_N with $\tilde{I}_1=[x_0+l,x_1]$ and $\tilde{I}_N=(x_{N-1},x_N-l]$, respectively. We choose the function $v_h(x,t)=\sum_{i=0}^{N}v_i(t)\phi_i(x,t)$ in the finite element space V_h^t to approximate the velocity $v(x,t)$. Denote by $\mathbf{v}=(v_0(t),...,v_N(t))^T$. We then can calculate the discrete dissipation function

$$\begin{aligned}\Phi_h(\mathbf{H},\mathbf{x};\mathbf{v})=&\int_{\tilde{I}_1}\frac{v_h(x,t)^2}{2H_h(x,t)}dx+\sum_{k=2}^{N-1}\int_{I_k}\frac{v_h(x,t)^2}{2H_h(x,t)}dx+\int_{\tilde{I}_N}\frac{v_h(x,t)^2}{2H_h(x,t)}dx\\&+\frac{1}{6\cos^2\theta_g^a}\mathcal{F}_h(\theta_d^a)\dot{x}_0^2+\frac{1}{6\cos^2\theta_g^b}\mathcal{F}_h(\theta_d^b)\dot{x}_N^2,\end{aligned}\tag{3.4}$$

where $\mathcal{F}_h$ represents the discrete function obtained by replacing the function $H(x,t)$ in equation (2.23) with $H_h(x,t)$. Since l is a parameter associated with the meso-scale, we assume that $l\ll h$, i.e., the mesh size is much larger than l. Notice that the parameter also appears in the form of $\mathcal{F}_h$, where $\zeta=l/l_c$.

Assume that the internal free knots move with velocity v_h in the Lagrange frame, i.e.

$$\dot{x}_i(t)=v_h(x_i,t),i=0,...,N.\tag{3.5}$$

Then the time derivative of $\mathcal{E}_h$ in (3.3) can be rewritten as

$$\dot{\mathcal{E}}_h(\mathbf{H},\mathbf{x};\dot{\mathbf{H}},\mathbf{v})=\sum_{i=1}^{N-1}\frac{\partial\mathcal{E}_h}{\partial H_i}\dot{H}_i+\sum_{i=0}^{N}\frac{\partial\mathcal{E}_h}{\partial x_i}v_i.$$

By the Onsager variational principle, $(\dot{\mathbf{H}},\mathbf{v})$ is obtained by solving the following problem

$$\begin{aligned}&\min_{\dot{\mathbf{H}},\mathbf{v}}\mathcal{R}_h(\mathbf{H},\mathbf{x};\dot{\mathbf{H}},\mathbf{v}):=\Phi_h(\mathbf{H},\mathbf{x};\mathbf{v})+\dot{\mathcal{E}}_h(\mathbf{H},\mathbf{x};\dot{\mathbf{H}},\mathbf{v})\\&s.t.\quad\int_I(\partial_t H_h+\partial_x(H_hv_h))w_hdx=0,\quad\forall w_h\in V_h^t.\end{aligned}\tag{3.6}$$

Notice that the continuous equation is satisfied in weak form.

We introduce a discrete Lagrangian multiplier $\lambda_h=\sum_{i=0}^{N}\lambda_i\phi_i(x,t)$ to deal with the constraint in the above problem. Then, the discrete modified Rayleighian functional is given by

$$\tilde{\mathcal{R}}_h=\Phi_h+\dot{\mathcal{E}}_h-\int_I(\partial_t H_h+\partial_x(H_hv_h))\lambda_hdx.\tag{3.7}$$

Under proper assumptions, the problem (3.6) is equivalent to the Euler-Lagrange equation corresponding to $\tilde{\mathcal{R}}_h$, i.e.

$$\begin{cases}\frac{\partial\mathcal{E}_h}{\partial H_i}-\int_I\phi_i\lambda_hdx=0, & i=1,...,N-1;\\ \int_I\frac{v_h\phi_i}{H_h}dx+\frac{\partial\mathcal{E}_h}{\partial x_i}-\int_I(\psi_i+\phi_i\partial_xH_h+H_h\partial_x\phi_i)\lambda_hdx=0, & i=1,...,N-1;\\ \int_{\tilde{I}}\frac{v_h\phi_0}{H_h}dx+\frac{\mathcal{F}_h(\theta_d^a)}{3\cos^2\theta_g^a}v_0+\frac{\partial\mathcal{E}_h}{\partial x_0}-\int_I(\psi_0+\phi_0\partial_xH_h+H_h\partial_x\phi_0)\lambda_hdx=0,\\ \int_{\tilde{I}}\frac{v_h\phi_N}{H_h}dx+\frac{\mathcal{F}_h(\theta_d^b)}{3\cos^2\theta_g^b}v_N+\frac{\partial\mathcal{E}_h}{\partial x_N}-\int_I(\psi_N+\phi_N\partial_xH_h+H_h\partial_x\phi_N)\lambda_hdx=0,\\ \int_I(\partial_tH_h+\partial_x(H_hv_h))\phi_idx=0, & i=0,...,N.\end{cases}\tag{3.8}$$

Due to the relationship $\dot{\mathbf{x}}=\mathbf{v}$, the equation (3.8) can be expressed in the following algebraic form

$$\begin{cases} \mathbf{M}(\mathbf{x}(t))\boldsymbol{\lambda}(t)=\frac{\partial \mathcal{E}_h}{\partial \mathbf{H}}(\mathbf{x}(t),\mathbf{H}(t)), \\ \mathbf{D}(\mathbf{x}(t),\mathbf{H}(t))\dot{\mathbf{x}}(t)=-\frac{\partial \mathcal{E}_h}{\partial \mathbf{x}}(\mathbf{x}(t),\mathbf{H}(t))+\mathbf{C}(\mathbf{x}(t),\boldsymbol{æ}(t))\boldsymbol{\lambda}(t), \\ \mathbf{M}^T(\mathbf{x}(t))\dot{\mathbf{H}}(t)+\mathbf{C}^T(\mathbf{x}(t),\mathbf{H}(t))\dot{\mathbf{x}}(t)=0, \end{cases} \tag{3.9}$$

where $\mathbf{M}\in\mathbb{R}^{N-1,N+1}$, $\mathbf{D}\in\mathbb{R}^{N+1,N+1}$, $\mathbf{C}\in\mathbb{R}^{N+1,N+1}$

$$\begin{aligned} M_{ij}(\mathbf{x}(t)) &= \int_{I(t)} \phi_i\phi_j dx; \\ C_{ij}(\mathbf{x}(t),\mathbf{H}(t)) &= \int_{I(t)} H_h\partial_x\phi_i\phi_j dx; \\ D_{ij}(\mathbf{x}(t),\mathbf{H}(t)) &= \int_{\tilde{I}(t)} \frac{\phi_i\phi_j}{H_h}dx+\delta_{i0}\delta_{0j}\frac{\mathcal{F}_h(\theta_d^a)}{3\cos^2\theta_g^a}+\delta_{iN}\delta_{Nj}\frac{\mathcal{F}_h(\theta_d^b)}{3\cos^2\theta_g^b}. \end{aligned}$$

Here δ_{ij} is equal to 1 if $i=j$ and equal to 0 otherwise. Therefore, we obtain the semi-discrete numerical scheme (3.8) or (3.9).

Similar to the assumptions in [60], we impose the following conditions: (a) The intervals $I_i(t),i=1,...,N$ are well-defined, i.e., $x_{i-1}(t)<x_i(t)$; and (b) The discrete density function $\mathbf{H}(t)$ is non-negative for all t. Under these assumptions, it can be readily verified that the discrete energy calculated by the semi-discrete numerical scheme always decays with respect to time.

Proposition 3.1. Let $(\mathbf{H}(t),\mathbf{x}(t))$ be the solution of the equations (3.8), and $H_h(t,x)\in V_h^t$ be the corresponding piecewise linear function. Under the above assumptions (a) and (b), we have

$$\frac{\partial \mathcal{E}_h(H_h)}{\partial t}\leq 0. \tag{3.10}$$

In addition, one also has the mass conservation property $\frac{d}{dt}\int_{x_0}^{x_N} H_h dx=0$.

Proof. The mass conservation is directly from the last equation in (3.8) by adding it for i from 0 to N. For the energy decaying property, it follows from the equations (3.3) and

(3.8) that

$$\begin{aligned}
\frac{\partial \mathcal{E}_h(H_h)}{\partial t} &= \sum_{i=1}^{N-1} \frac{\partial \mathcal{E}_h}{\partial \rho_i} \dot{H}_i + \sum_{i=0}^{N} \frac{\partial \mathcal{E}_h}{\partial x_i} \dot{x}_i \\
&= \sum_{i=0}^{N} \int_I \phi_i \lambda_h dx \dot{H}_i + \sum_{i=1}^{N-1} \Big(\int_I (H_h \partial_x \phi_i) \lambda_h dx - \int_I \frac{v_h \phi_i}{H_h} dx \Big) v_i \\
&\quad + \Big(\int_I (H_h \partial_x \phi_0) \lambda_h dx - \int_{\tilde{I}} \frac{v_h \phi_0}{H_h} dx - \frac{\mathcal{F}_h(\theta_d^a)}{3\cos^2 \theta_g^a} v_0 \Big) v_0 \\
&\quad + \Big(\int_I (H_h \partial_x \phi_N) \lambda_h dx - \int_{\tilde{I}} \frac{v_h \phi_N}{H_h} dx - \frac{\mathcal{F}_h(\theta_d^b)}{3\cos^2 \theta_g^b} v_N \Big) v_N \\
&= \sum_{i=0}^{N} \Big(\int_I \partial_t H_h \phi_i dx + \int_I \partial_x (H_h v_h) \phi_i dx \Big) \lambda_i - \sum_{i=1}^{N-1} \int_{I_i} \frac{v_h \phi_i}{H_h} dx v_i \\
&\quad - \int_{\tilde{I}_0} \frac{v_h \phi_0}{H_h} dx v_0 - \int_{\tilde{I}_N} \frac{v_h \phi_N}{H_h} dx v_N - \frac{\mathcal{F}_h(\theta_d^a)}{3\cos^2 \theta_g^a} v_0^2 - \frac{\mathcal{F}_h(\theta_d^b)}{3\cos^2 \theta_g^b} v_N^2 \\
&= -2\Phi_h(\mathbf{H}, \mathbf{x}; \mathbf{v}) \leq 0.
\end{aligned}$$

This proves (3.10) as desired. □

3.2 Full Discretization

In order to obtain the fully discrete numerical scheme, we need introduce appropriate temporal discretizations for the semi-discrete numerical scheme. Let the time step be τ , then we set the solution at $t = t^n$ as $H_i^n = H_i(t^n), x_i^n = x_i(t^n)$, and the solution at t^{n+1} as H_i^{n+1}, x_i^{n+1}. We define the finite difference operator $\bar{\partial} H^n = (H^{n+1} - H^n)/\tau$ and then $v_i^{n+1} = \bar{\partial} x_i^n = (x_i^{n+1} - x_i^n)/\tau$. We first consider an explicit Euler scheme as follows

$$\int_{I^n} \phi_i^n \lambda_h^{n+1} dx = \frac{\partial \mathcal{E}_h^n}{\partial H_i^n}, \qquad i = 1, ..., N-1; \tag{3.11}$$

$$\int_{\tilde{I}^n} \frac{v_h^{n+1} \phi_i^n}{H_h^n} dx = -\frac{\partial \mathcal{E}_h^n}{\partial x_i^n} + \int_{I^n} H_h^n \partial_x \phi_i^n \lambda_h^{n+1} dx, \qquad i = 1, ..., N-1; \tag{3.12}$$

$$\int_{\tilde{I}^n} \frac{v_h^{n+1} \phi_0^n}{H_h^n} dx + \frac{\mathcal{F}_h(\theta_d^a)}{3\cos^2 \theta_g^a} v_0^{n+1} = -\frac{\partial \mathcal{E}_h^n}{\partial x_0^n} + \int_{I^n} H_h^n \partial_x \phi_0^n \lambda_h^{n+1} dx, \tag{3.13}$$

$$\int_{\tilde{I}^n} \frac{v_h^{n+1} \phi_N^n}{H_h^n} dx + \frac{\mathcal{F}_h(\theta_d^b)}{3\cos^2 \theta_g^b} v_N^{n+1} = -\frac{\partial \mathcal{E}_h^n}{\partial x_0^n} + \int_{I^n} H_h^n \partial_x \phi_N^n \lambda_h^{n+1} dx, \tag{3.14}$$

$$\int_{I^n}\Big(\sum_{j=1}^{N-1}\bar{\delta}H_j^n\phi_j^n\Big)\phi_i^n=-\int_{I^n}\Big(\sum_{j=0}^{N}v_j^{n+1}\psi_j^n\Big)\phi_i^n dx-\int_{I^n}\partial_x(H_h^n v_h^{n+1})\phi_i^n dx,\quad i=0,...,N. \tag{3.15}$$

Here $I^n=(x_0^n,x_N^n)$ and $\tilde{I}_n=(x_0^n+l,x_N^n-l)$. The fully discrete numerical scheme can be rewritten in the matrix form

$$\begin{cases}\mathbf{M}(\mathbf{x}^n)\boldsymbol{\lambda}^{n+1}=\frac{\partial\mathcal{E}_h}{\partial\mathbf{H}}(\mathbf{x}^n,\mathbf{H}^n),\\ \mathbf{D}(\mathbf{x}^n,\mathbf{H}^n)\bar{\delta}\mathbf{x}^n-\mathbf{C}(\mathbf{x}^n,\mathbf{H}^n)\boldsymbol{\lambda}^{n+1}=-\frac{\partial\mathcal{E}_h}{\partial\mathbf{x}}(\mathbf{x}^n,\mathbf{H}^n),\\ \mathbf{M}^T(\mathbf{x}^n)\bar{\delta}\mathbf{H}^n+\mathbf{C}^T(\mathbf{x}^n,\mathbf{H}^n)\bar{\delta}\mathbf{x}^n=0.\end{cases} \tag{3.16}$$

Notice that $\boldsymbol{\lambda}_h^{n+1}$ and M is not a square matrix. As a consequence, the matrix system (3.23) is coupled, precluding a sequential solution for $\boldsymbol{\lambda},\dot{\mathbf{x}}$ and $\dot{\mathbf{H}}$. Since the thin film equation is a nonlinear fourth-order partial differential equation, the explicit Euler scheme necessitates selecting an appropriately small time step τ to maintain numerical stability.

To improve computational efficiency, we design a stabilized semi-implicit discrete scheme. When $t=t^{n+1}$, we perform a Taylor expansion of the terms $\frac{\partial\mathcal{E}_h}{\partial\mathbf{H}}(\mathbf{x}(t),\mathbf{H}(t))$ and $\frac{\partial\mathcal{E}_h}{\partial\mathbf{x}}(\mathbf{x}(t),\mathbf{H}(t))$ at the point $(\mathbf{x}^n,\mathbf{H}^n)$, i.e.,

$$\begin{aligned}\frac{\partial\mathcal{E}_h}{\partial\mathbf{H}}(\mathbf{x}^{n+1},\mathbf{H}^{n+1})&\approx\frac{\partial\mathcal{E}_h}{\partial\mathbf{H}}(\mathbf{x}^n,\mathbf{H}^n)+\tau\frac{\partial^2\mathcal{E}_h}{\partial\mathbf{H}\partial\mathbf{x}}(\mathbf{x}^n,\mathbf{H}^n)\bar{\delta}\mathbf{x}^n+\tau\frac{\partial^2\mathcal{E}_h}{\partial\mathbf{H}^2}(\mathbf{x}^n,\mathbf{H}^n)\bar{\delta}\mathbf{H}^n,\\ \frac{\partial\mathcal{E}_h}{\partial\mathbf{x}}(\mathbf{x}^{n+1},\mathbf{H}^{n+1})&\approx\frac{\partial\mathcal{E}_h}{\partial\mathbf{x}}(\mathbf{x}^n,\mathbf{H}^n)+\tau\frac{\partial^2\mathcal{E}_h}{\partial\mathbf{x}\partial\mathbf{H}}(\mathbf{x}^n,\mathbf{H}^n)\bar{\delta}\mathbf{H}^n+\tau\frac{\partial^2\mathcal{E}_h}{\partial\mathbf{x}^2}(\mathbf{x}^n,\mathbf{H}^n)\bar{\delta}\mathbf{x}^n.\end{aligned}$$

Replace the right hand terms in equation (3.23) by the above expansions, we obtain the following stabilized semi-implicit discrete scheme

$$\begin{cases}\mathbf{M}(\mathbf{x}^n)\boldsymbol{\lambda}^{n+1}-\tau\frac{\partial^2\mathcal{E}_h}{\partial\mathbf{H}\partial\mathbf{x}}\bar{\delta}\mathbf{x}^n-\tau\frac{\partial^2\mathcal{E}_h}{\partial\mathbf{H}^2}\bar{\delta}\mathbf{H}^n=\frac{\partial E_h}{\partial\mathbf{H}}(\mathbf{x}^n,\mathbf{H}^n),\\ \tau\frac{\partial^2\mathcal{E}_h}{\partial\mathbf{x}\partial\mathbf{H}}\bar{\delta}\mathbf{H}^n+\Big(\tau\frac{\partial^2\mathcal{E}_h}{\partial\mathbf{x}^2}+\mathbf{D}(\mathbf{x}^n,\mathbf{H}^n)\Big)\bar{\delta}\mathbf{x}^n-\mathbf{C}(\mathbf{x}^n,\mathbf{H}^n)\boldsymbol{\lambda}^{n+1}\\ \qquad\qquad=-\frac{\partial\mathcal{E}_h}{\partial\mathbf{x}}(\mathbf{x}^n,\mathbf{H}^n),\\ \mathbf{M}^T(\mathbf{x}^n)\bar{\delta}\mathbf{H}^n+\mathbf{C}^T(\mathbf{x}^n,\mathbf{H}^n)\bar{\delta}\mathbf{x}^n=0.\end{cases} \tag{3.17}$$

We expect that the stabilized scheme is much more stable than the explicit Euler scheme. This will be verified by the numerical experiments in the next section.

3.3 Full Discretization

In order to obtain the fully discrete numerical scheme, we need introduce appropriate temporal discretizations for the semi-discrete numerical scheme. Let the time step be τ , then we set the solution at $t=t^n$ as $H_i^n=H_i(t^n),x_i^n=x_i(t^n)$, and the solution at t^{n+1}

as H_i^{n+1},x_i^{n+1}. We define the finite difference operator $\bar{\partial}H^n=(H^{n+1}-H^n)/\tau$ and then $v_i^{n+1}=\bar{\partial}x_i^n=(x_i^{n+1}-x_i^n)/\tau$. We first consider an explicit Euler scheme as follows

$$\int_{I^n}\phi_i^n\lambda_h^{n+1}dx=\frac{\partial\mathcal{E}_h^n}{\partial H_i^n},\qquad i=1,...,N-1; \tag{3.18}$$

$$\int_{\tilde{I}^n}\frac{v_h^{n+1}\phi_i^n}{H_h^n}dx=-\frac{\partial\mathcal{E}_h^n}{\partial x_i^n}+\int_{I^n}H_h^n\partial_x\phi_i^n\lambda_h^{n+1}dx,\qquad i=1,...,N-1; \tag{3.19}$$

$$\int_{\tilde{I}^n}\frac{v_h^{n+1}\phi_0^n}{H_h^n}dx+\frac{\mathcal{F}_h(\theta_d^a)}{3\cos^2\theta_g^a}v_0^{n+1}=-\frac{\partial\mathcal{E}_h^n}{\partial x_0^n}+\int_{I^n}H_h^n\partial_x\phi_0^n\lambda_h^{n+1}dx, \tag{3.20}$$

$$\int_{\tilde{I}^n}\frac{v_h^{n+1}\phi_N^n}{H_h^n}dx+\frac{\mathcal{F}_h(\theta_d^b)}{3\cos^2\theta_g^b}v_N^{n+1}=-\frac{\partial\mathcal{E}_h^n}{\partial x_0^n}+\int_{I^n}H_h^n\partial_x\phi_N^n\lambda_h^{n+1}dx, \tag{3.21}$$

$$\int_{I^n}\Big(\sum_{j=1}^{N-1}\bar{\partial}H_j^n\phi_j^n\Big)\phi_i^n=-\int_{I^n}\Big(\sum_{j=0}^{N}v_j^{n+1}\psi_j^n\Big)\phi_i^n dx-\int_{I^n}\partial_x(H_h^nv_h^{n+1})\phi_i^n dx,\qquad i=0,...,N. \tag{3.22}$$

Here $I^n=(x_0^n,x_N^n)$ and $\tilde{I}_n=(x_0^n+l,x_N^n-l)$. The fully discrete numerical scheme can be rewritten in the matrix form

$$\begin{cases}\mathbf{M}(\mathbf{x}^n)\boldsymbol{\lambda}^{n+1}=\frac{\partial\mathcal{E}_h}{\partial\mathbf{H}}(\mathbf{x}^n,\mathbf{H}^n),\\ \mathbf{D}(\mathbf{x}^n,\mathbf{H}^n)\bar{\partial}\mathbf{x}^n-\mathbf{C}(\mathbf{x}^n,\mathbf{H}^n)\boldsymbol{\lambda}^{n+1}=-\frac{\partial\mathcal{E}_h}{\partial\mathbf{x}}(\mathbf{x}^n,\mathbf{H}^n),\\ \mathbf{M}^T(\mathbf{x}^n)\bar{\partial}\mathbf{H}^n+\mathbf{C}^T(\mathbf{x}^n,\mathbf{H}^n)\bar{\partial}\mathbf{x}^n=0.\end{cases} \tag{3.23}$$

Notice that $\boldsymbol{\lambda}_h^{n+1}$ and M is not a square matrix. As a consequence, the matrix system (3.23) is coupled, precluding a sequential solution for $\boldsymbol{\lambda}$,$\dot{\mathbf{x}}$ and $\dot{\mathbf{H}}$. Since the thin film equation is a nonlinear fourth-order partial differential equation, the explicit Euler scheme necessitates selecting an appropriately small time step τ to maintain numerical stability.

To improve computational efficiency, we design a stabilized semi-implicit discrete scheme. When $t=t^{n+1}$, we perform a Taylor expansion of the terms $\frac{\partial\mathcal{E}_h}{\partial\mathbf{H}}(\mathbf{x}(t),\mathbf{H}(t))$ and $\frac{\partial\mathcal{E}_h}{\partial\mathbf{x}}(\mathbf{x}(t),\mathbf{H}(t))$ at the point $(\mathbf{x}^n,\mathbf{H}^n)$, i.e.,

$$\begin{aligned}\frac{\partial\mathcal{E}_h}{\partial\mathbf{H}}(\mathbf{x}^{n+1},\mathbf{H}^{n+1})&\approx\frac{\partial\mathcal{E}_h}{\partial\mathbf{H}}(\mathbf{x}^n,\mathbf{H}^n)+\tau\frac{\partial^2\mathcal{E}_h}{\partial\mathbf{H}\partial\mathbf{x}}(\mathbf{x}^n,\mathbf{H}^n)\bar{\partial}\mathbf{x}^n+\tau\frac{\partial^2\mathcal{E}_h}{\partial\mathbf{H}^2}(\mathbf{x}^n,\mathbf{H}^n)\bar{\partial}\mathbf{H}^n,\\ \frac{\partial\mathcal{E}_h}{\partial\mathbf{x}}(\mathbf{x}^{n+1},\mathbf{H}^{n+1})&\approx\frac{\partial\mathcal{E}_h}{\partial\mathbf{x}}(\mathbf{x}^n,\mathbf{H}^n)+\tau\frac{\partial^2\mathcal{E}_h}{\partial\mathbf{x}\partial\mathbf{H}}(\mathbf{x}^n,\mathbf{H}^n)\bar{\partial}\mathbf{H}^n+\tau\frac{\partial^2\mathcal{E}_h}{\partial\mathbf{x}^2}(\mathbf{x}^n,\mathbf{H}^n)\bar{\partial}\mathbf{x}^n.\end{aligned}$$

Replace the right hand terms in equation (3.23) by the above expansions, we obtain the

following stabilized semi-implicit discrete scheme

$$\begin{cases} \mathbf{M}(\mathbf{x}^n)\boldsymbol{\lambda}^{n+1} - \tau\dfrac{\partial^2\mathcal{E}_h}{\partial\mathbf{H}\partial\mathbf{x}}\bar{\partial}\mathbf{x}^n - \tau\dfrac{\partial^2\mathcal{E}_h}{\partial\mathbf{H}^2}\bar{\partial}\mathbf{H}^n = \dfrac{\partial E_h}{\partial\mathbf{H}}(\mathbf{x}^n,\mathbf{H}^n), \\ \tau\dfrac{\partial^2\mathcal{E}_h}{\partial\mathbf{x}\partial\mathbf{H}}\bar{\partial}\mathbf{H}^n + \Big(\tau\dfrac{\partial^2\mathcal{E}_h}{\partial\mathbf{x}^2} + \mathbf{D}(\mathbf{x}^n,\mathbf{H}^n)\Big)\bar{\partial}\mathbf{x}^n - \mathbf{C}(\mathbf{x}^n,\mathbf{H}^n)\boldsymbol{\lambda}^{n+1} \\ \qquad\qquad = -\dfrac{\partial\mathcal{E}_h}{\partial\mathbf{x}}(\mathbf{x}^n,\mathbf{H}^n), \\ \mathbf{M}^T(\mathbf{x}^n)\bar{\partial}\mathbf{H}^n + \mathbf{C}^T(\mathbf{x}^n,\mathbf{H}^n)\bar{\partial}\mathbf{x}^n = 0. \end{cases} \tag{3.24}$$

We expect that the stabilized scheme is much more stable than the explicit Euler scheme. This will be verified by the numerical experiments in the next section.

4 Numerical Examples

In this section, we will present some numerical results on the fourth-order thin film equation with moving contact lines. We first test the convergence and stability of the numerical schemes. Then we show that the scheme can be used to simulate the thin film dynamics on both flat and rough substrates.

4.1 Convergence Test

Since the analytical solution of the fourth-order thin film equation (2.32) remains unknown, we first consider the following simplified fourth-order model, namely the Hele-Shaw equation:

$$\partial_t H + \partial_x(H\partial_{xxx}H) = 0. \tag{4.1}$$

This equation is primarily used to describe the flow of two immiscible fluids in a Hele-Shaw cell [1]. It is shown that equation (4.1) has a radially symmetric, compactly supported self-similar solution [11, 65], given by

$$H(x,t) = \frac{1}{24\alpha}(C - x^2\alpha^{-2})_+^2, \tag{4.2}$$

where $\alpha = [5(t+t_0)]^{1/5}$ and the constant C is determined by the total mass of the initial condition. For the Hele-Shaw equation, we can specify its corresponding free energy

$$E = \int_{I(t)} \frac{1}{2}(\partial_x H)^2 dx,$$

and dissipation function

$$\Phi = \int_{I(t)} \frac{1}{2} H v^2 dx.$$

Notice that the dissipation function is well-defined over the region $I(t)$ where the droplet is in contact with the substrate, and no singularity arises at the moving boundary. By combining homogeneous Dirichlet boundary condition with the mass conservation constraint, we can similarly derive the Hele-Shaw equation (4.1) using the Onsager variational principle. The resulting variational structure enables the application of the same discretization strategies, yielding the explicit Euler scheme (3.23) and the stabilized semi-implicit scheme (3.24). To assess the accuracy of the numerical methods, we perform convergence tests using the known exact self-similar solution. At the final simulation time T, the error in the L^2 norm between the numerical solution H_h and the analytical solution H is computed as

$$err_{L^2} := \Big(\int_{I(T)} (H(x,T) - H_h(x,T))^2 dx \Big)^{\frac{1}{2}}.$$

Taking the self-similar solution (4.2) with parameters $t_0 = 1.5$ and $C = 4$ as the initial condition, and setting the final time $T = 2$, we assess the numerical performance of both the explicit and stabilized semi-implicit schemes. As shown in Tables 1 and 2, both methods exhibit second-order convergence in the L^2 norm. However, the choice of time step size has a pronounced impact on the performance of the schemes. The time step for the explicit Euler scheme needs to be sufficiently small to ensure numerical stability, whereas the stabilized semi-implicit scheme has much less stringent requirements on the time step size. This enhanced stability arises from the fact that the stabilized semi-implicit method serves as a consistent approximation to the fully implicit scheme and thus is much more stable than the explicit scheme. To improve computational efficiency, all subsequent numerical simulations in this section are carried out using the stabilized semi-implicit scheme.

Table 1: The convergence rate of explicit Euler method.

Number	τ	L^2-error	Order
12	$\frac{1}{10000}$	6.4859×10^{-3}	
24	$\frac{1}{40000}$	1.7649×10^{-3}	1.8778
48	$\frac{1}{160000}$	4.7666×10^{-4}	1.8886
96	$\frac{1}{640000}$	1.1266×10^{-4}	2.0810

Table 2: The convergence rate of stabilized semi-implicit method.

Number	τ	L^2-error	Order
12	$\frac{1}{10}$	6.7422×10^{-3}	
24	$\frac{1}{40}$	1.8957×10^{-3}	1.8305
48	$\frac{1}{160}$	4.7617×10^{-4}	1.9932
96	$\frac{1}{640}$	1.1732×10^{-4}	2.0210

It is worth noting that the stabilized semi-implicit scheme (3.24) does not strictly preserve total mass. To evaluate the extent of mass loss, we consider the same initial condition given by the self-similar solution (4.2) with $t_0 = 1.5$ and $C = 4$, and set the final time $T = 2$, at which point the total mass is 1.4222. As shown in Table 3, the error in total numeircal mass exhibits a second-order convergence rate with respect to the mesh size.

Table 3: The convergence rate of numerical mass at $T = 2$.

Number	τ	Error of numerical mass	Order
12	$\frac{1}{10}$	1.0612×10^{-3}	
24	$\frac{1}{40}$	2.6076×10^{-4}	2.0249
48	$\frac{1}{160}$	6.3130×10^{-5}	2.0463
96	$\frac{1}{640}$	1.5359×10^{-5}	2.0392

4.2 Dynamic Wetting on a Flat Substrate

In this subsection, we investigate the dynamic wetting behavior of a droplet on a flat substrate, corresponding to the case where the roughness function satisfies $R(x) = 0$. Let $\theta_Y = 1$, $l = 10^{-6}$, and $l_c = 10^{-10}$, with $\ln\zeta = \ln(l/l_c)$. The initial shape of the droplet is denoted as

$$H(x) = 1 - x^2. \tag{4.3}$$

Assuming that gravitational effects and external forces are negligible, i.e., $B_o = 0$ and $B_x = 0$, the evolution of the droplet is governed solely by capillary forces. Under these conditions, the evolution of the droplet profile and the velocity of the contact lines are depicted in Figure 3. As illustrated in Figure 3(a), the droplet undergoes spreading driven by capillary forces, expanding both vertically and laterally until it reaches an equilibrium configuration. Meanwhile, the contact line velocities $\dot{x}_a$ and $\dot{x}_b$ converge to zero, as shown in Figure 3(b).

Figure 4 presents the numerical simulation results for the droplet evolution under the combined effects of capillary forces and gravity, with parameters set as $B_o = 1$ and $B_x = 0$, while other conditions remain unchanged. Compared to the capillary forces-dominated case, the presence of gravity significantly alters the droplet dynamics and final configuration. The droplet spreads more extensively and attains a lower stationary state height, reflecting the competition between surface tension, which favors curvature-driven contraction, and gravity, which promotes flattening by redistributing mass downward.

Figure 5 illustrates the numerical simulation of a droplet subjected to capillary forces, gravity, and an additional horizontal external force, with $B_o = 1$ and $B_x = 0.5$. The results show that the droplet gradually deforms and eventually evolves into a traveling wave that moves rightward at a constant speed [42]. This steady propagation reflects a balance between capillary-driven surface tension, gravitational spreading, and horizontal forcing. In particular, capillary forces tend to minimize surface curvature, promoting spreading, while the external force introduces a persistent directional motion that breaks

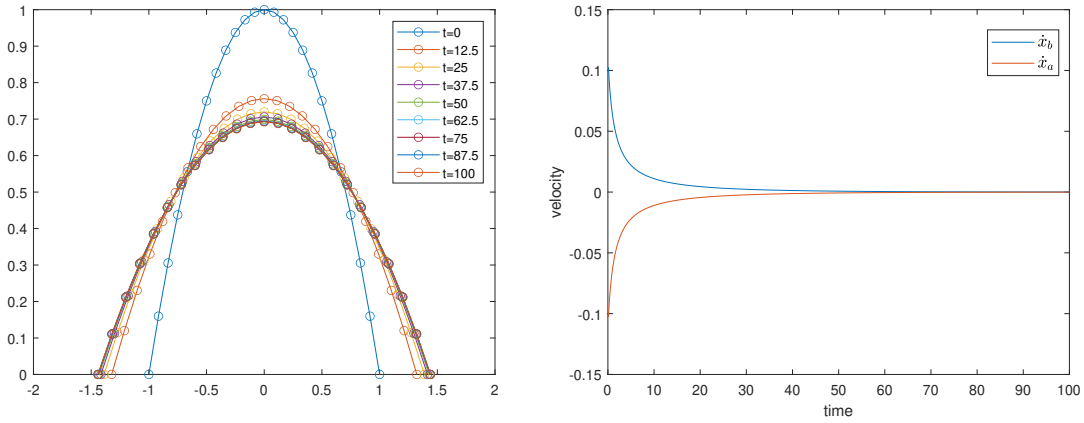

(a) Temporal evolution of droplet profiles (b) The velocity of the contact lines

Figure 3: Temporal evolution of droplet for $B_o = 0$ and $B_x = 0$ on a flat surface.

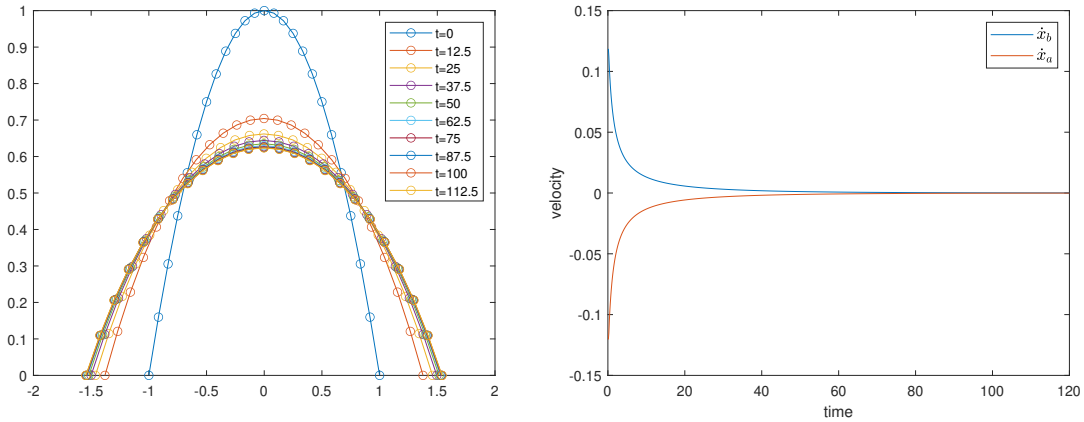

(a) Temporal evolution of droplet profiles (b) The velocity of the contact lines

Figure 4: Temporal evolution of droplet for $B_o = 1$ and $B_x = 0$ on a flat surface.

the symmetry of the shape. Gravity contributes to lowering the center of mass and suppressing height, thereby enhancing lateral extension.

When the external force increases to $B_x = 0.8$, as illustrated in Figure 6, the droplet develops a more pronounced asymmetry characterized by a thin trailing film and a pronounced capillary ridge at the front. This behavior arises from the nonlinear competition between capillarity and strong external forcing: while capillary forces resist sharp gradients and promote smoother profiles, the stronger horizontal force continuously pulls

fluid forward, generating a sharp front and leaving a thin layer behind. The overall footprint of the droplet increases significantly, indicating transition into the so-called "large-droplet" regime described by Benilov and Benilov [66]. This transition underscores the sensitivity of wetting dynamics to external driving, and highlights the capability of the proposed model to capture complex interfacial phenomena in forced spreading scenarios.

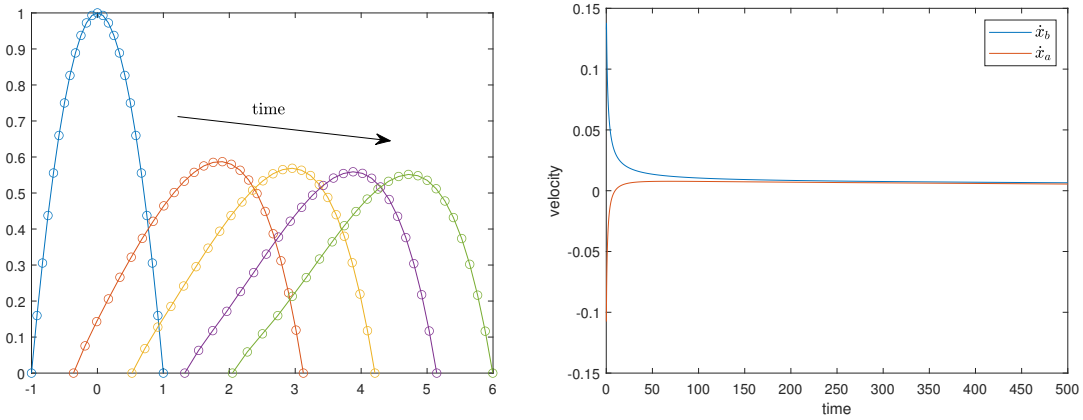

(a) Temporal evolution of droplet profiles (b) The velocity of the contact lines

Figure 5: Temporal evolution of droplet for $B_o = 1$ and $B_x = 0.5$ on a flat surface.

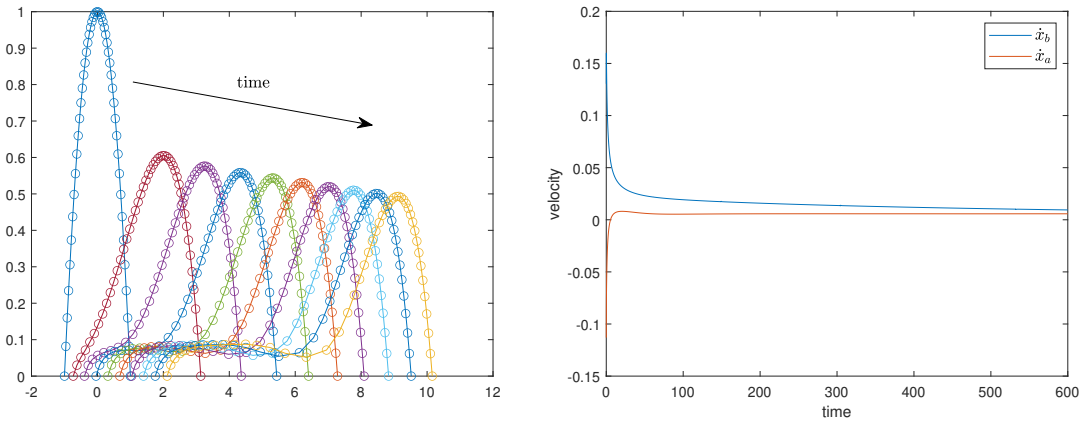

(a) Temporal evolution of droplet profiles (b) The velocity of the contact lines

Figure 6: Temporal evolution of droplet for $B_o = 1$ and $B_x = 0.8$ on a flat surface.

Finally, we investigate the spatial convergence behavior of the numerical model at a fixed time. Specifically, we consider the case with $B_o = 1$ and $B_x = 0.5$, while maintaining all other initial conditions unchanged. The droplet is evolved from the initial state up to the final time $T = 20$. As shown in Figure 7, the computed droplet profiles exhibit consistent convergence as the spatial mesh is refined. This demonstrates the robustness and accuracy of the proposed numerical scheme in capturing the long-time behavior of the system under the combined effects of capillarity, gravity, and external forcing.

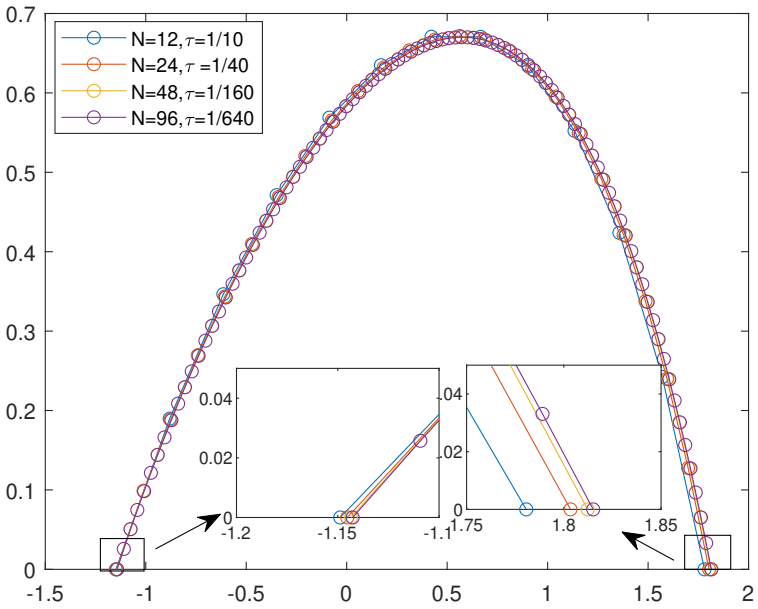

Figure 7: The convergence of model at $T = 20$.

4.3 Effectiveness of the macroscopic boundary conditions

To further assess the robustness of the macroscopic boundary condition and to elucidate the roles played by different dissipation mechanisms, we conduct a series of numerical tests focusing on the meso-scale wedge region adjacent to the moving contact line on a flat substrate.

We consider a sliding liquid film along a substrate under gravity and an external force in the x direction. We set $Bo = 1$ and $Bx = 0.8$. The other parameters are chosen as in Section 4.2. We consider two situations: with and without using the macroscopic boundary condition. In the latter case, we simply set $\mathcal{F}(\theta_d) = \alpha$ instead of the expression in (2.23). In both cases, we test two different choices for the parameter l, i.e., $l = 10^{-2}$ and $l = 10^{-7}$. Some typical results are shown in Figure 8.

Firstly, Figure 8(a) shows the profile of the film in different cases at $t=20$. We observe that without using the macroscopic boundary condition, the film advances much more rapidly than in the case with the condition. This discrepancy is most pronounced for $l=10^{-2}$, since the dissipation in the wedge region near the contact line is neglected. The discrepancy becomes smaller when a smaller parameter $l=10^{-7}$ is chosen. This indicates that the results are very sensitive to the choice of the parameter l in this scenario. On the other hand, when the macroscopic boundary condition is used, the numerical results are close to each other whether we set $l=10^{-2}$ or $l=10^{-7}$. In other words, the numerical results are robust with respect to the choice of l when the macroscopic boundary condition is employed. This is because the dissipation in the wedge region is included in the macroscopic boundary condition and because the parameter ζ in (2.23) also depends on l.

Figure 8(b) shows the long-time profiles of the film at $t=100$. The results are similar and even more pronounced. Without using the macroscopic boundary condition, the solution for $l=10^{-2}$ fails to develop the characteristic front–ridge and rear–film morphology associated with driven thin-film flows. In contrast, when using the macroscopic boundary condition, the correct morphological structure emerges for both values of l, and the resulting profiles remain close despite a five-order-of-magnitude difference in l.

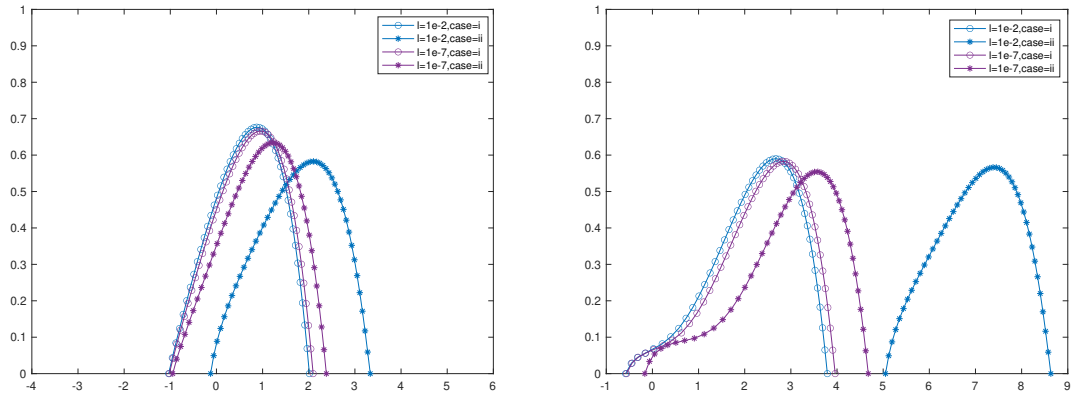

(a) Droplet profiles at $t=20$

(b) Droplet profiles at $t=100$

Figure 8: Comparison of droplet profiles for different dissipation configurations under gravity and external forcing ($Bo=1, Bx=0.8$).

Overall, the numerical experiments reported herein lead to two key conclusions. First, the dissipation in the meso-scale wedge region plays a crucial role in the motion of the contact line. Without the macroscopic model, one must choose a very small cut-off parameter l. On the other hand, our macroscopic model incorporates wedge-region dissipation. As a result, the numerical scheme exhibits strong robustness with respect to the

choice of l, even when its value varies by several orders of magnitude. These findings highlight the advantages of the modeling framework adopted in this work.

4.4 Dynamic Wetting on a Rough Substrate

This subsection investigates the wetting dynamics of a droplet on rough substrates, where the substrate profile satisfies $R(x)\neq 0$. Let $\theta_Y=1$, $l=10^{-6}$, and $l_c=10^{-10}$, with $\ln\zeta=\ln(l/l_c)$. The initial shape of the droplet is prescribed by (4.3), and the substrate roughness is described by

$$R(x)=\frac{1}{10}\sin(5x). \tag{4.4}$$

We first consider the case where the droplet dynamics is governed solely by capillarity, i.e., $B_o=0$ and $B_x=0$. As shown in Figure 9, the droplet undergoes initial spreading and eventually reaches a stationary equilibrium configuration. This behavior is qualitatively similar to that observed on flat substrates, although the final shape is modulated by the underlying topography.

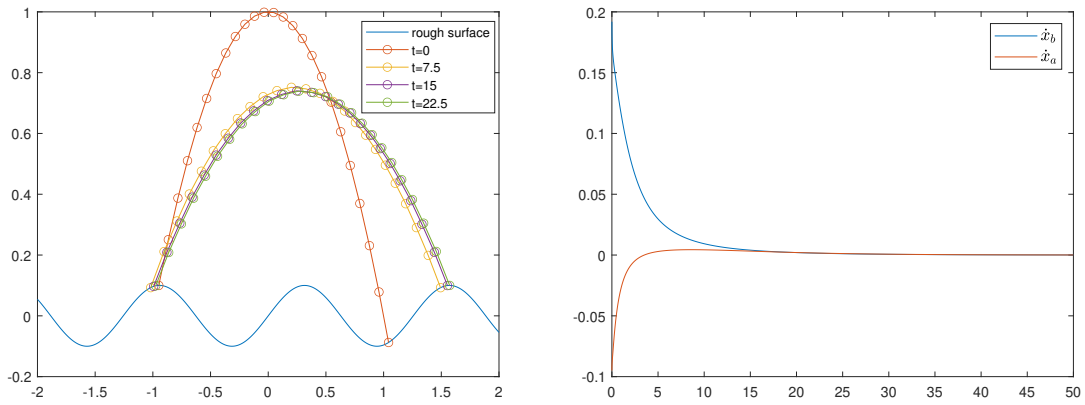

(a) Temporal evolution of droplet profiles

(b) The velocity of the contact lines

Figure 9: Temporal evolution of droplet for $B_o=0$ and $B_x=0$ on a rough surface.

Subsequently, we consider the shape evolution of the droplet under the influence of capillary forces, gravity, and external forces. For $B_o=1$ and $B_x=0.5$, the droplet deforms and evolves toward a pinned equilibrium state, as illustrated in Figure 10. The roughness-induced pinning effect prevents sustained motion, under moderate external forcing in x direction.

To explore the transition beyond pinning, we increase the external force to $B_x=0.8$. The substrate and initial droplet configurations remain the same as in (4.4) and (4.3). The droplet evolves from time zero to $T=1200$, as depicted in Figure 11(a). During this

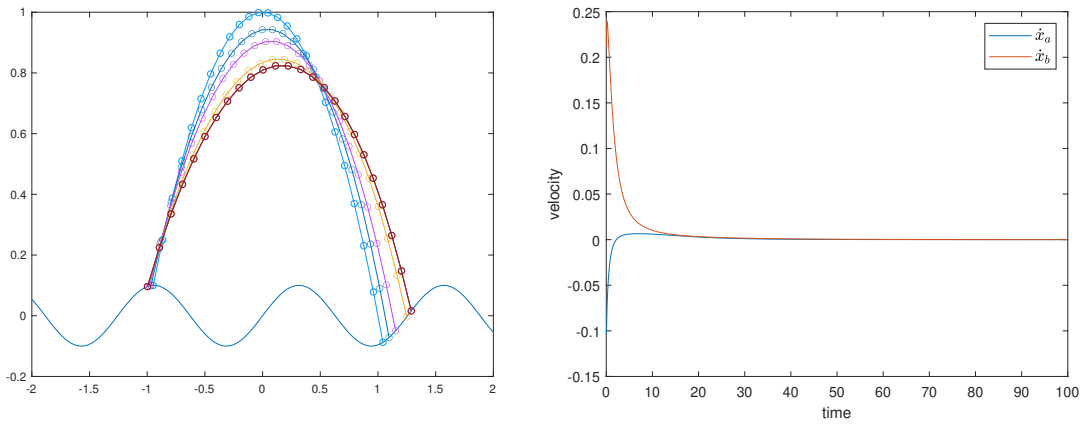

(a) Temporal evolution of droplet profiles

(b) The velocity of the contact lines

Figure 10: Temporal evolution of droplet for $B_o = 1$ and $B_x = 0.5$ on a rough surface.

process, the droplet shape becomes increasingly asymmetric, and contact angle hysteresis is observed. The temporal evolution of the apparent contact angles θ_a and θ_b is shown in Figure 11(c), while the corresponding contact line velocities and positions are reported in Figures 11(b) and 11(d), respectively. These results reflect the dynamic wetting resistance induced by substrate roughness and the nonlinear coupling between contact line motion and substrate geometry.

Further increasing the external force to $B_x = 1$ yields enhanced droplet mobility, as shown in Figure 12. In this regime, the droplet advances more rapidly, and significant deformation occurs at the receding edge. Notably, the rear contact line can exhibit negative apparent contact angles when interacting with negatively sloped substrate regions, as demonstrated in Figure 12(b).

To explore the influence of substrate roughness, we consider a new substrate profile $R(x) = \frac{1}{100}\sin(10x)$, with the initial droplet shape described by (4.3), and parameters $B_o = 1$ and $B_x = 1$. As shown in Figure 13(a), the droplet eventually develops a traveling-wave-like profile reminiscent of the "large droplet" regime on flat substrates. Contact angle hysteresis persists, as evidenced in Figure 13(b), although its magnitude is diminished. The reduced roughness scale introduces multiscale features at the contact line, which poses additional challenges for numerical resolution and requires finer discretization to accurately capture the localized wetting behavior.

5 Conclusion

This study investigates the dynamic wetting behavior of droplets on rough substrates. Utilizing the Onsager variational principle as an approximation tool, we systematically

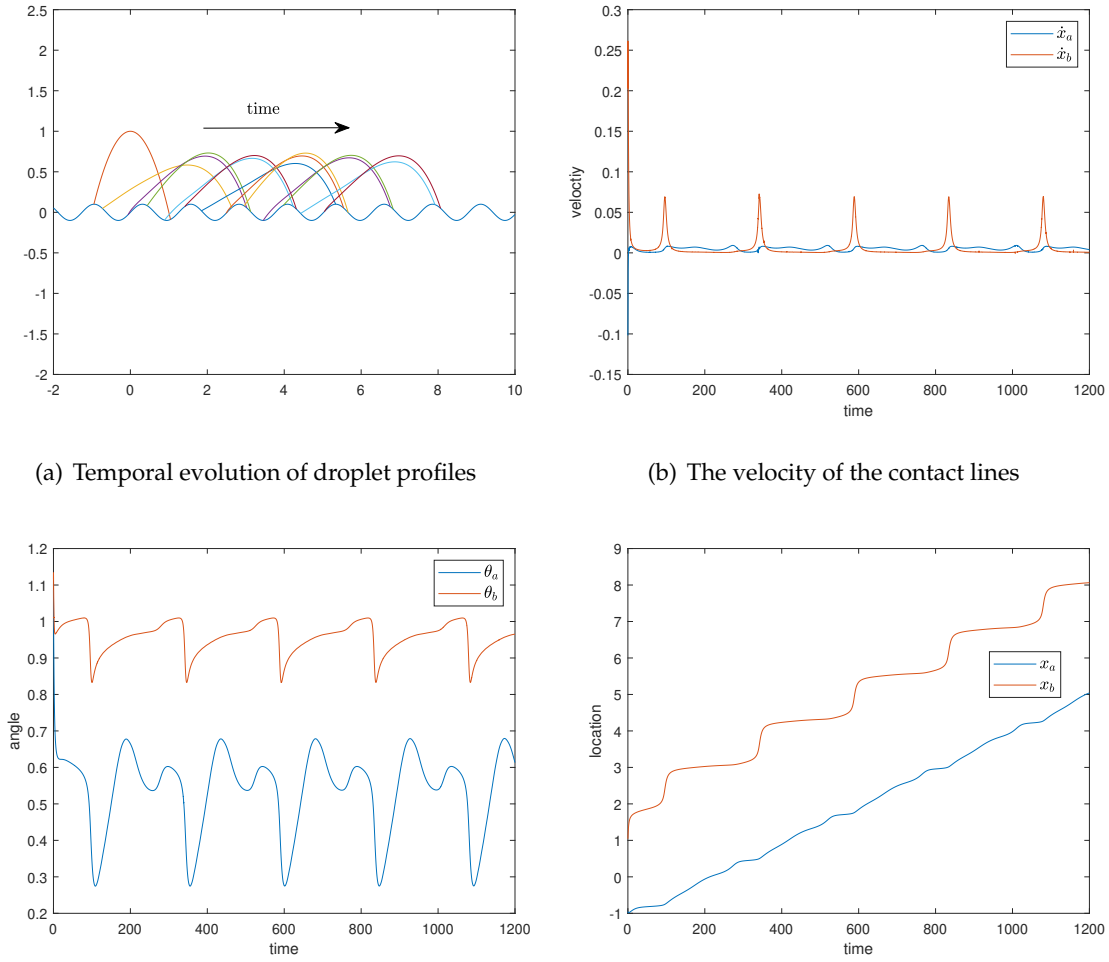

(a) Temporal evolution of droplet profiles

(b) The velocity of the contact lines

(c) The contact angles hysteresis

(d) The location of contact lines

Figure 11: Temporal evolution of droplet for $B_o = 1$ and $B_x = 0.8$ on a rough surface.

derive a reduced fourth-order nonlinear thin film model (2.32), accompanied by appropriate dynamic boundary conditions that account for contact line motion. Building on the discrete Onsager variational principle and inspired by recent advances in the numerical treatment of porous medium equation [60], we developed an explicit numerical scheme and further proposed a stabilized semi-implicit scheme. Numerical results indicate that both schemes achieve second-order accuracy in the L^2 norm. Notably, the semi-implicit approach effectively relaxes the stringent time step constraints typically encountered in the numerical solution of fourth-order nonlinear PDEs. A series of simulations were conducted to explore the interplay between capillarity, gravity, and external forcing in

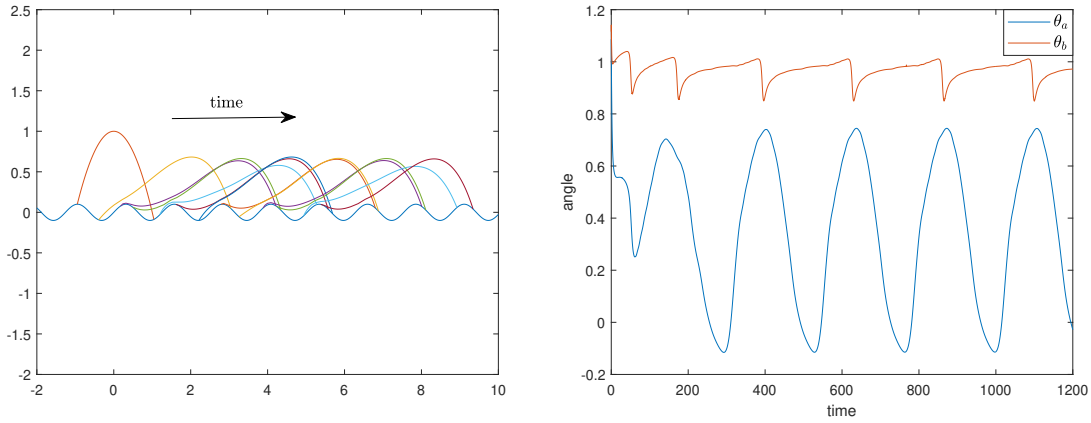

(a) Temporal evolution of droplet profiles (b) The contact angles hysteresis

Figure 12: Temporal evolution of droplet for $B_o = 1$ and $B_x = 1$ on a rough surface.

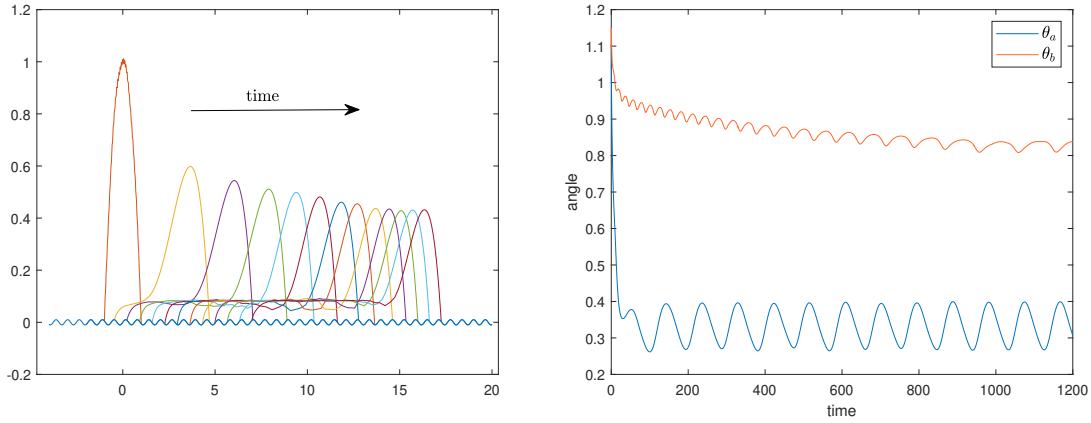

(a) Temporal evolution of droplet profiles (b) The contact angles hysteresis

Figure 13: Temporal evolution of droplet for $B_o = 1$ and $B_x = 1$ on a rough surface.

driving droplet dynamics on rough surfaces. The results capture several key physical features, including the transition from symmetric spreading to directional transport, the onset of contact angle hysteresis under strong external forces, and the emergence of pinning effects due to substrate roughness. These findings are consistent with theoretical predictions and prior studies, and they underscore the capability of the proposed variational framework to accurately model complex interfacial phenomena.

Due to the intrinsic coupling between temporal and spatial scales in free boundary

problems, accurately resolving the motion of the moving contact line necessitates careful adjustment of the time step, particularly as substrate roughness reduces gradually. In the limit of vanishing roughness, the numerical resolution of the associated thin film equation becomes increasingly stiff and computationally demanding. To address this challenge, future research will aim to incorporate coarse-grained or effective boundary models that capture the macroscopic influence of microscale substrate features, as exemplified in [67], thereby enabling efficient and accurate simulations of droplet wetting on complex surfaces.

Acknowledgments

The work was partially supported by the National Key R&D Program of China (No.2024YFA1012502) the National Natural Science Foundation of China (No. 12371415, 12461160275), and the Natural Science Foundation of Beijing Municipality (No. Z240001).

References

[1] A. Oron, S. H. Davis, S. G. Bankoff, Long-scale evolution of thin liquid films, Reviews of Modern Physics 69 (3) (1997) 931.
[2] P.-G. de Gennes, F. Brochard-Wyart, D. Quéré, Capillarity and Wetting Phenomena: Drops, Bubbles, Pearls, Waves, Springer, 2004.
[3] D. Bonn, J. Eggers, J. Indekeu, J. Meunier, E. Rolley, Wetting and spreading, Reviews of Modern Physics 81 (2) (2009) 739–805.
[4] S. Kumar, Liquid transfer in printing processes: liquid bridges with moving contact lines, Annual Review of Fluid Mechanics 47 (1) (2015) 67–94.
[5] P. Constantin, T. F. Dupont, R. E. Goldstein, L. P. Kadanoff, M. J. Shelley, S.-M. Zhou, Droplet breakup in a model of the Hele-Shaw cell, Physical Review E 47 (6) (1993) 4169.
[6] T. F. Dupont, R. E. Goldstein, L. P. Kadanoff, S.-M. Zhou, Finite-time singularity formation in Hele-Shaw systems, Physical Review E 47 (6) (1993) 4182.
[7] A. I. Pesci, R. E. Goldstein, M. J. Shelley, Domain of convergence of perturbative solutions for Hele-Shaw flow near interface collapse, Physics of Fluids 11 (10) (1999) 2809–2811.
[8] G. I. Barenblatt, Scaling, Self-similarity, and Intermediate Asymptotics: Dimensional Analysis and Intermediate Asymptotics, Cambridge University Press, 1996.
[9] Z. Li, W. Ren, The motion of a thin drop on an elastic sheet, Journal of Fluid Mechanics 1022 (2025) A4.
[10] F. Bernis, A. Friedman, Higher order nonlinear degenerate parabolic equations, Journal of Differential Equations 83 (1) (1990) 179–206.
[11] R. Ferreira, F. Bernis, Source-type solutions to thin-film equations in higher dimensions, European Journal of Applied Mathematics 8 (5) (1997) 507–524.
[12] A. L. Bertozzi, The mathematics of moving contact lines in thin liquid films, Notices of the AMS 45 (6) (1998) 689–697.
[13] A. L. Bertozzi, M. Pugh, The lubrication approximation for thin viscous films: Regularity and long-time behavior of weak solutions, Communications on Pure and Applied Mathematics 49 (2) (1996) 85–123.

[14] J. Evans, V. Galaktionov, J. King, Blow-up similarity solutions of the fourth-order unstable thin film equation, European Journal of Applied Mathematics 18 (2) (2007) 195–231.
[15] P. Álvarez-Caudevilla, V. A. Galaktionov, Well-posedness of the Cauchy problem for a fourth-order thin film equation via regularization approaches, Nonlinear Analysis: Theory, Methods & Applications 121 (2015) 19–35.
[16] L. Giacomelli, H. Knüpfer, A free boundary problem of fourth order: classical solutions in weighted Hölder spaces, Communications in Partial Differential Equations 35 (11) (2010) 2059–2091.
[17] F. Otto, Lubrication approximation with prescribed nonzero contact anggle, Communications in Partial Differential Equations 23 (11-12) (1998) 2077–2164.
[18] M. Bertsch, L. Giacomelli, G. Karali, Thin-film equations with "partial wetting" energy: existence of weak solutions, Physica D: Nonlinear Phenomena 209 (1-4) (2005) 17–27.
[19] L. Zhornitskaya, A. L. Bertozzi, Positivity-preserving numerical schemes for lubrication-type equations, SIAM Journal on Numerical Analysis 37 (2) (1999) 523–555.
[20] G. Grün, M. Rumpf, Nonnegativity preserving convergent schemes for the thin film equation, Numerische Mathematik 87 (1) (2000) 113–152.
[21] C. Huh, L. Scriven, Hydrodynamic model of steady movement of a solid/liquid/fluid contact line, Journal of Colloid and Interface Science 35 (1) (1971) 85–101.
[22] S. H. Davis, E. B. Dussan, On the motion of a fluid-fluid interface along a solid surface, Journal of Fluid Mechanics 65 (1) (1974) 71–95.
[23] J. Eggers, Contact line motion for partially wetting fluids, Physical Review E 72 (6) (2005) 061605.
[24] L. M. Pismen, J. Eggers, Solvability condition for the moving contact line, Physical Review E 78 (5) (2008) 056304.
[25] L. M. Pismen, Y. Pomeau, Disjoining potential and spreading of thin liquid layers in the diffuse-interface model coupled to hydrodynamics, Physical Review E 62 (2) (2000) 2480.
[26] L. Schwartz, D. Roux, J. Cooper-White, On the shapes of droplets that are sliding on a vertical wall, Physica D: Nonlinear Phenomena 209 (1-4) (2005) 236–244.
[27] U. Thiele, K. Neuffer, M. Bestehorn, Y. Pomeau, M. G. Velarde, Sliding drops on an inclined plane, Colloids and Surfaces A: Physicochemical and Engineering Aspects 206 (1-3) (2002) 87–104.
[28] H. P. Greenspan, On the motion of a small viscous droplet that wets a surface, Journal of Fluid Mechanics 84 (1) (1978) 125–143.
[29] R. Cox, The dynamics of the spreading of liquids on a solid surface. Part 1. Viscous flow, Journal of Fluid Mechanics 168 (1986) 169–194.
[30] M. Zhou, P. Sheng, Dynamics of immiscible-fluid displacement in a capillary tube, Physical Review Letters 64 (8) (1990) 882.
[31] P. J. Haley, M. J. Miksis, The effect of the contact line on droplet spreading, Journal of Fluid Mechanics 223 (1991) 57–81.
[32] L. Hocking, The spreading of a thin drop by gravity and capillarity, The Quarterly Journal of Mechanics and Applied Mathematics 36 (1) (1983) 55–69.
[33] J. Eggers, Hydrodynamic theory of forced dewetting, Physical Review Letters 93 (9) (2004) 094502.
[34] T. Qian, X.-P. Wang, P. Sheng, Molecular scale contact line hydrodynamics of immiscible flows, Physical Review E 68 (1) (2003) 016306.
[35] T. Qian, X.-P. Wang, P. Sheng, A variational approach to moving contact line hydrodynamics, Journal of Fluid Mechanics 564 (2006) 333–360.

[36] W. Ren, et al., Boundary conditions for the moving contact line problem, Physics of fluids 19 (2) (2007).
[37] W. Ren, E. Weinan, Contact line dynamics on heterogeneous surfaces, Physics of Fluids 23 (7) (2011).
[38] S. Engelnkemper, M. Wilczek, S. V. Gurevich, U. Thiele, Morphological transitions of sliding drops: Dynamics and bifurcations, Physical Review Fluids 1 (7) (2016) 073901.
[39] J. A. Diez, L. Kondic, Computing three-dimensional thin film flows including contact lines, Journal of Computational Physics 183 (1) (2002) 274–306.
[40] M. Norouzisadeh, P. Leroy, C. Soulaine, A lubrication model with slope-dependent disjoining pressure for modeling wettability alteration, Computer Physics Communications 298 (2024) 109114.
[41] P. Sun, R. D. Russell, J. Xu, A new adaptive local mesh refinement algorithm and its application on fourth order thin film flow problem, Journal of Computational Physics 224 (2) (2007) 1021–1048.
[42] D. Peschka, Thin-film free boundary problems for partial wetting, Journal of Computational Physics 295 (2015) 770–778.
[43] D. Peschka, L. Heltai, Model hierarchies and higher-order discretisation of time-dependent thin-film free boundary problems with dynamic contact angle, Journal of Computational Physics 464 (2022) 111325.
[44] J. Qin, W. Lu, P. Gao, A numerical method for dynamic wetting using mesoscopic contact-line models, Communications in Computational Physics 36 (2024) 977–995.
[45] L. Hocking, Sliding and spreading of thin two-dimensional drops, The Quarterly Journal of Mechanics and Applied Mathematics 34 (1) (1981) 37–55.
[46] N. Savva, S. Kalliadasis, Two-dimensional droplet spreading over topographical substrates, Physics of Fluids 21 (9) (2009).
[47] S. Wilson, R. Hunt, B. Duffy, The rate of spreading in spin coating, Journal of Fluid Mechanics 413 (2000) 65–88.
[48] N. Savva, D. Groves, S. Kalliadasis, Droplet dynamics on chemically heterogeneous substrates, Journal of Fluid Mechanics 859 (2019) 321–361.
[49] L. Onsager, Reciprocal relations in irreversible processes. I., Physical Review 37 (4) (1931) 405.
[50] L. Onsager, Reciprocal relations in irreversible processes. II., Physical Review 38 (12) (1931) 2265.
[51] M. Doi, Onsager priciple as a tool for approximation, Chinese Phys. B 24 (2015) 020505.
[52] X. Xu, Y. Di, M. Doi, Variational method for contact line problems in sliding liquids, Physics of Fluids 28 (8) (2016) 087101.
[53] X. Man, M. Doi, Ring to mountain transition in deposition pattern of drying droplets, Physical Review Letters 116 (6) (2016) 066101.
[54] J. Zhou, Y. Jiang, M. Doi, Cross interaction drives stratification in drying film of binary colloidal mixtures, Physical Review Letters 118 (10) (2017) 108002.
[55] M. Doi, J. Zhou, Y. Di, X. Xu, Application of the Onsager-Machlup integral in solving dynamic equations in nonequilibrium systems, Physical Review E 99 (6) (2019) 063303.
[56] S. Guo, X. Xu, T. Qian, Y. Di, M. Doi, P. Tong, Onset of thin film meniscus along a fibre, Journal of Fluid Mechanics 865 (2019) 650–680.
[57] Z. Zhang, X. Xu, Effective boundary conditions for dynamic contact angle hysteresis on chemically inhomogeneous surfaces, Journal of Fluid Mechanics 935 (2022).
[58] S. Lu, X. Xu, An efficient diffusion generated motion method for wetting dynamics, Journal

of Computational Physics 441 (2021) 110476.
[59] X. Xu, A variational analysis for the moving finite element method for gradient flows, Journal of Computational Mathematics 41 (2) (2023) 191–210.
[60] S. Xiao, X. Xu, A moving mesh method for porous medium equation by the onsager variational principle, Journal of Computational Physics (2025) 114061.
[61] Y. Liu, X. Xu, A variational discretization method for mean curvature flows by the Onsager principle, CSIAM Transactions on Applied Mathematics 6 (1) (2025) 63–95.
[62] X. Xu, X. Wang, Theoretical analysis for dynamic contact angle hysteresis on chemically patterned surfaces, Physics of Fluids 32 (11) (2020).
[63] S. Guo, M. Gao, X. Xiong, Y. J. Wang, X. Wang, P. Sheng, P. Tong, Direct measurement of friction of a fluctuating contact line, Physical Review Letters 111 (2) (2013) 026101.
[64] V. A. Galaktionov, S. R. Svirshchevskii, Exact solutions and invariant subspaces of nonlinear partial differential equations in mechanics and physics, Chapman and Hall/CRC, 2006.
[65] N. F. Smyth, J. M. Hill, High-order nonlinear diffusion, IMA Journal of Applied Mathematics 40 (2) (1988) 73–86.
[66] E. Benilov, M. Benilov, A thin drop sliding down an inclined plate, Journal of Fluid Mechanics 773 (2015) 75–102.
[67] S. Xiao, X. Xu, Z. Zhang, Multiscale analysis for dynamic contact angle hysteresis on rough surfaces, Multiscale Modeling & Simulation 21 (1) (2023) 400–425.